Development of a Platform for Sensing Cellular Electrical Activity Using Nitrogen Vacancy Centers in Nanodiamonds

by

Anubhav Sinha

S.B., EECS and Chemistry, Massachusetts Institute of Technology (2014)

Submitted to the Department of Electrical Engineering and Computer Science

in partial fulfillment of the requirements for the degree of

Master of Engineering in Electrical Engineering and Computer Science

at the

MASSACHUSETTS INSTITUTE OF TECHNOLOGY

September 2015

Signature redacted

Author .....

Department of Electrical Engineering and Computer Science

September 8, 2015

Signature redacted

Certified by. .....

Prof. Dirk R. Englund

Jamieson Career Development Assistant Professor

Thesis Supervisor

Signature redacted

Accepted by .. ..

Dr. Christopher J. Terman

Chairman, Masters of Engineering Thesis Committee

Development of a Platform for Sensing Cellular Electrical Activity Using Nitrogen Vacancy Centers in Nanodiamonds

by

Anubhav Sinha

Submitted to the Department of Electrical Engineering and Computer Science
on September 8, 2015, in partial fulfillment of the
requirements for the degree of
Master of Engineering in Electrical Engineering and Computer Science

Abstract

The nitrogen vacancy center (NV) in diamond hosts unique optical properties that allows it to be used for sensing magnetic fields, electric fields, and temperature. In addition, the photostability of the NV center and the biocompatibility of diamond suggests the utility of the NV center for biosensing. The dependence of the charge state of the NV center on the local electrochemical environment suggests that the NV center could be used as an optical sensor for electrophysiology.

In this thesis, a platform to evaluate the utility of the NV center for voltage sensing is established. First, an electrophysiology setup is built and characterized on HEK293 cells. The setup adds functionality to a home built microscope so that cells can be electrically controlled while simultaneously observing the fluorescence. Second, the staining of neurons with hydrogen-terminated nanodiamonds (NDs) with NV centers is improved. Together, the improved staining of neurons with nanodiamonds along with using the electrophysiology setup to observe modulation forms a platform for future study of the NV center as a voltage sensor.

Thesis Supervisor: Prof. Dirk R. Englund
Title: Jamieson Career Development Assistant Professor

Acknowledgments

I would like to express my sincere gratitude to Professor Dirk Englund for all of his guidance and support throughout my time in the lab.

I would especially like to thank Sinan Karaveli for his extensive mentorship throughout my project. I would also like to thank the rest of the Quantum Photonics Laboratory for all of their help both inside and out of the lab.

My project has been a highly collaborative one and I am extremely grateful for having had great collaborators in the Boyden Lab. I am especially grateful to Or Shemesh for hands-on help with all aspects of my project.

Finally, I would like to thank my parents for their unyielding love and support.

Contents

List of Figures

List of Tables

Chapter 1

Introduction

The functional activity of the nervous system in higher organisms leads to emergent complex behaviors. The connectome, the complete map of neural connections within the brain, provides the "wiring diagram" for information in the form of action potentials to be carried and processed [1]. These networks are incredibly complex with about 10^{11} neurons in the adult human brain and over 10^{15} synapses between neurons. Information processing through this highly interconnected network is responsible for complex processes [1].

To understand how a complex network of neurons processes information, tools are needed to interrogate the structural connectivity of the neurons as well as the dynamics of action potential propagation through the network [2]. An ideal tool to study a living brain would allow for simultaneous structural identification of neurons at sufficient resolution to resolve synapses (20-40 nm in size) as well as simultaneous detection of electrical activity [3]. Currently, no such methods exist. To study the structure of the connectome, high throughput electron microscopy has been successful but suffers from the limitation of requiring extensive sample processing and fixation [4] [5]. Super-resolution methods such as STORM/PALM have also shown success in tracing neural paths and offer the advantage of color multiplexing [6] [7].

The dynamics of single neurons within larger networks has been studied in great detail by intracellular electrode or patch clamp recordings. However, these methods are extremely challenging to scale in order to study an entire network simultaneously

[8]. To study neural networks, sensitive and noninvasive methods that operate at high spatiotemporal resolution over a large region are needed. The peak of an action potential is extremely brief, lasting 1 ms with voltage depolarization approximately 80–100 mV above the resting potential [9]. To capture these events, a reporter/detector system must be sufficiently sensitive to detect the action potential and report it at a frequency of 1 kHz. Such a method must also be able to discern action potentials between different neurons that are spatially close together. The invasiveness of a detection modality is an important factor affecting its scalability for studying a large ensemble of neurons [9]. Methods that are minimally toxic allow for longer recordings to be taken. The need to genetically engineer an organism or cell line is also a related metric of invasiveness.

Two main classes of methods are commonly used to make neuronal recordings: electrical and optical methods. Current electrical methods suffer from limitations in their scalability while most optical methods suffer from photobleaching, cytotoxicity, and limited spatiotemporal resolution.

The optical properties of the negatively charged nitrogen-vacancy center (NV^- center) center, a crystallographic defect in diamond, have been extensively studied for applications in quantum information science and nanoscale sensing [10] [11] [12]. The NV^- center has emerged as a highly sensitive nanoscale sensor for magnetic fields [13] [14] [15], electric fields [16] [17], and temperature [18], among other properties. Diamond is also a potentially biocompatible material that is minimally cytotoxic [19] [20]. Together, the sensing properties of diamond and its biocompatibility have aroused great interest in using the NV center for all-optical detection of neuronal action potentials [21] [22] [23].

In this thesis, a platform is developed to evaluate the utility of the NV center within nanodiamonds (NDs) for this purpose. Recent work has shown that NV centers within NDs modulate their charge state in response to an applied voltage [24]. This charge state switching is optically detectable as a change in fluorescence intensity when passed through a 650 nm longpass filter. Hydrogenated nanodiamonds have been shown to exhibit particularly large fluorescence changes ($\Delta F/F$), making them

of particular interest [24]. In addition to this, a technique for staining neurons with nanodiamonds has been recently developed [25].

For characterization of the NV center for sensing purposes, full electrical control of single cells labeled with NDs containing NV centers is needed while imaging changes in the the NV center fluorescence. To be able to carry out such an experiment, we developed two concurrent approaches. The first is building an electrophysiology rig around an existing homebuilt microscope and the second is effectively delivering the nanodiamonds of interest to the neurons.

In Chapter 2, fundamentals of electrophysiology and current state of the art techniques for sensing action potentials are outlined. In Chapter 3, the photophysics of the NV center are described. Chapter 4 details the design and characterization of the electrophysiology rig that was built. Chapter 5 describes the optimization and characterization of the neuronal labeling process. Chapter 6 summarizes the work and provides an outlook for future work. Figure 1-1 relates the work presented in Chapters 4 and 5 to the overall platform.

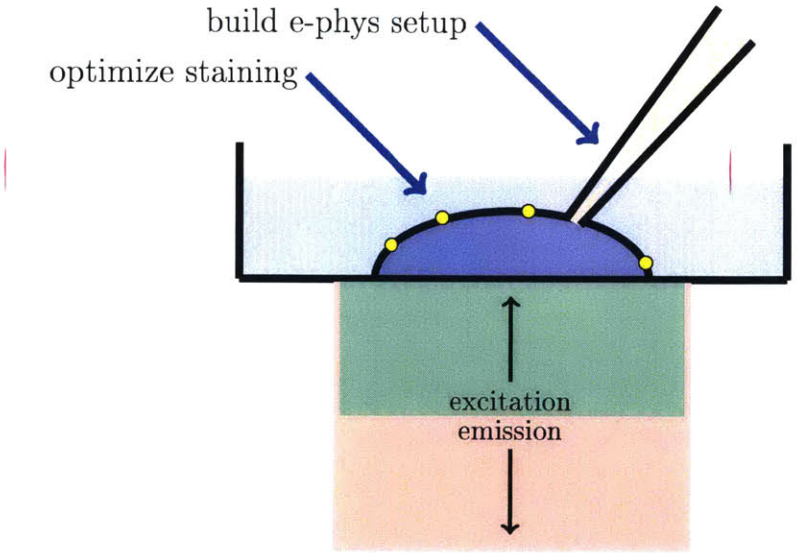

Figure 1-1: A schematic describing the specific work presented in this thesis within the overall platform. A cell has been stained with nanodiamonds (shown in yellow) and has been patch clamped (pipette shown in orange). The fluorescence from the nanodiamonds is recorded and is analyzed with the voltage measurements in order to determine the voltage-sensing ability of the NV center.

Chapter 2

Electrophysiology theory and current sensing methods

Electrophysiology encompasses a diverse set of methods and techniques used to study the electrical properties of cells and tissues. In this section, the fundamentals of neuronal electrophysiology are outlined in Section 2.1 and current methodology is reviewed in Section 2.2.

2.1 Cellular electrophysiology

Neurons code, transmit, integrate, and decode information in the form of action potentials, localized changes in the electrical membrane potential that propagate along neurons [3]. Most neurons follow an overall architecture for information flow. A cartoon drawing of a neuron and a brightfield image are shown in Figure 2-1.

A chemical signal at one of the dendrites is received and converted into an electrical signal. The signals from many dendrites are integrated at the cell body. If the total stimulus is strong enough to pass over the axon hillock, a positive-feedback process results in an action potential which is carried down the axon. The electrical signal is converted to a chemical signal at the nerve terminals of the axonal tree and passed on to the dendrites of a downstream cell at a chemical synapse [27].

The plasma membrane of a cell separates the cytoplasm from the extracellular

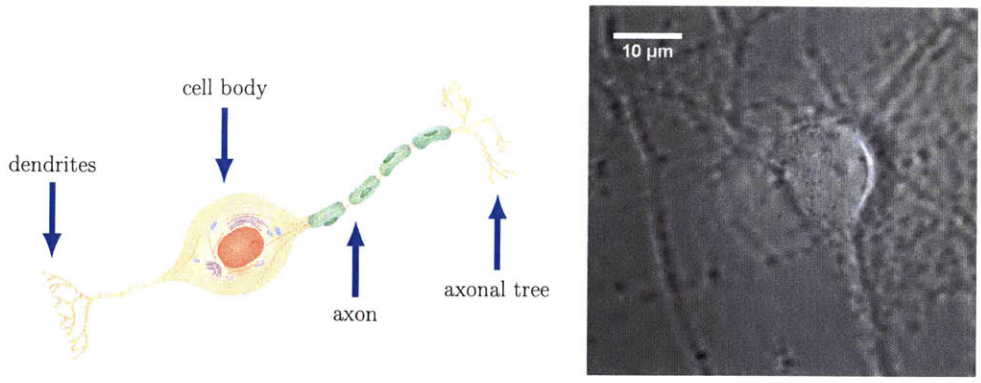

Figure 2-1: **Left.** The most significant anatomical features of a neuron are highlighted on this cartoon. Information arrives at the dendrites, is integrated at the cell body, is propagated down the axon, and is transmitted through the axonal tree. Figure adopted from [26]. **Right.** Bright-field image of a neuron taken with 100x magnification.

environment. Specialized membrane proteins are needed to allow for ion transport to occur. These proteins include ion channels that allow for ion-selective facilitated diffusion through a protein pore in the membrane as well as poreless transporters [27] [28]. Of particular relevance for electrophysiology are pumps that carry out active transport of molecules against their electrochemical gradient [27].

Ion	Intracellular concentration (mM)	Extracellular concentration
Na^+	5–20	130–160
K^+	130–160	4–8
Ca^{2+}	0.05 – 1	1.2 – 4
Cl^-	1–60	100–140

Table 2.1: Important ion gradients for electrophysiological phenomena. Adapted from [28].

The concentrations and fluxes of ions between the intracellular and extracellular environments result in an electrical potential across the membrane potential [27]. In physiological systems, the most important ions for electrical activity and their typical concentrations are given in Table 2.1 (adapted from [28]). There are many transport proteins that are responsible for producing the ion concentration gradient. The Na^+/K^+-ATPase pump is of particular note and is primarily responsible for the maintenance of the sodium and potassium ion gradients. In addition, there are also Na^+, K^+, and Cl^- leak channels (among others) that allow for facilitated diffusion

down the concentration gradients and create leakage currents that are very important in determining the membrane potential [27].

In the resting potential steady state, there are no net changes of ion concentrations. Every ion in solution has an associated membrane conductance that gives the ease for that species to pass through the membrane, an associated Nernst electrochemical potential from the concentration gradient, and a current density that is carried by the ion as it crosses the membrane [27]. In addition, there is an active current for each ion as well. A network circuit model can be built from which the membrane current density, membrane conductance, membrane capacitance, and membrane potential can be obtained [27]. In animal neurons, the resting membrane potential is typically in the range of -60 – -70 mV [28]. Figure 2-2 shows the most important transporters and their relative ion fluxes into/out of the cell along with the resting potential.

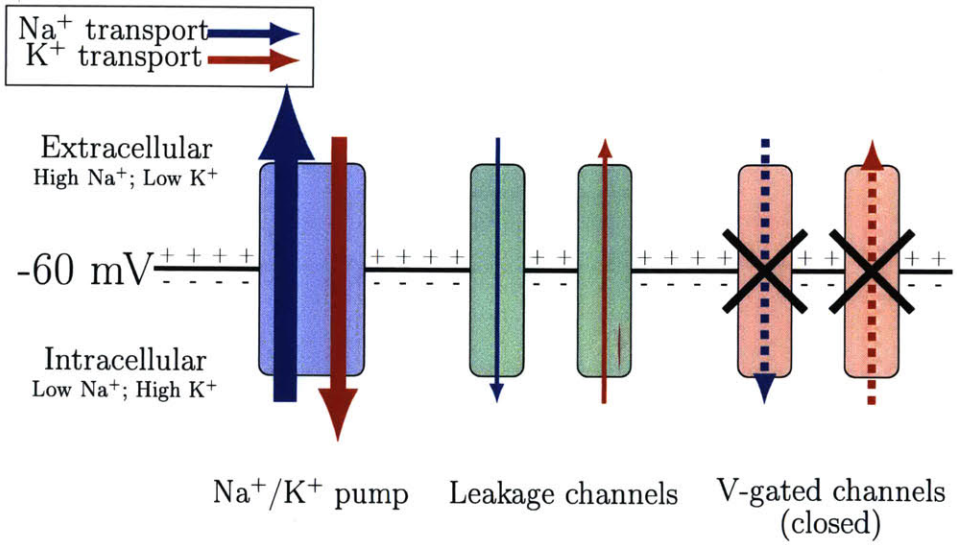

Figure 2-2: The Na^+/K^+ pump and leakage channels are constantly functional. When the membrane is at the resting potential, the voltage-gated channels are closed. Under membrane depolarization, the sodium influx channel opens first. After the membrane has sufficiently depolarized, the sodium influx channels become inactivated and the potassium channels open, beginning repolarization. Hyperpolarization is caused by the opening of additional potassium channels [27].

The key phenomena distinguishing the action potential from the resting potential (shown as stage 1 in Figure 2-3) is the fact that the membrane conductance to particular ions in neurons rapidly changes in response to changes in the local voltage. In

neurons, an electrical depolarization that crosses a certain threshold voltage leads to the opening of voltage-gated sodium channels allowing for influx of Na^+ that further depolarizes the membrane. As the membrane voltage increases, positive feedback rapidly causes more sodium channels to open, depolarizing the membrane potential to roughly 80–100 mV above the resting membrane potential (stage 2 in Figure 2-3). The sodium gates rapidly inactivate and Na^+ is transported out of the membrane. The depolarized membrane potential also causes voltage-gated K^+ channels to open, causing an efflux of K^+ to exit the cell. This restores the membrane potential towards the resting membrane potential (stage 3). Additional K^+ channels open during this phase leading to hyperpolarization of the cell membrane before restoration of the membrane potential to the resting value (stage 4) [28] [27]. The membrane potential change during the action potential depolarizes the adjacent part of the membrane and propagates the action potential; hyperpolarization ensures that propagation of the action potential is one-direction [27].

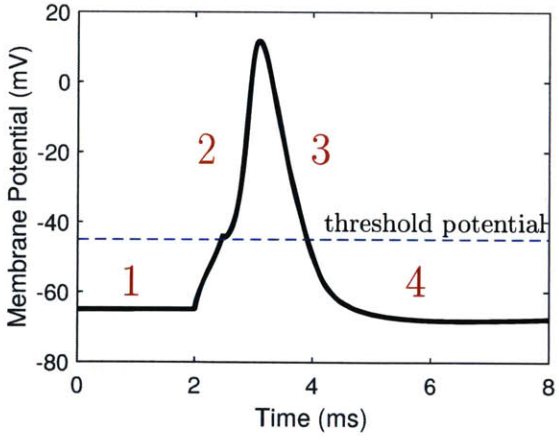

Figure 2-3: The four stages of the action potential are shown. Stage 1: initial membrane depolarization up to the threshold potential. Stage 2: rapid membrane depolarization due to Na^+ influx. Stage 3: Membrane repolarization due to K^+ efflux. Stage 4: Membrane hyperpolarization. Figure generated using NEURON software [29].

2.2 Current electrophysiology methods

Electrical and optical methods are the two primary classes of techniques used to study the dynamics of neuronal systems at cellular resolution [9]. Figure 2-4 summarizes the major methods used in cellular electrophysiology.

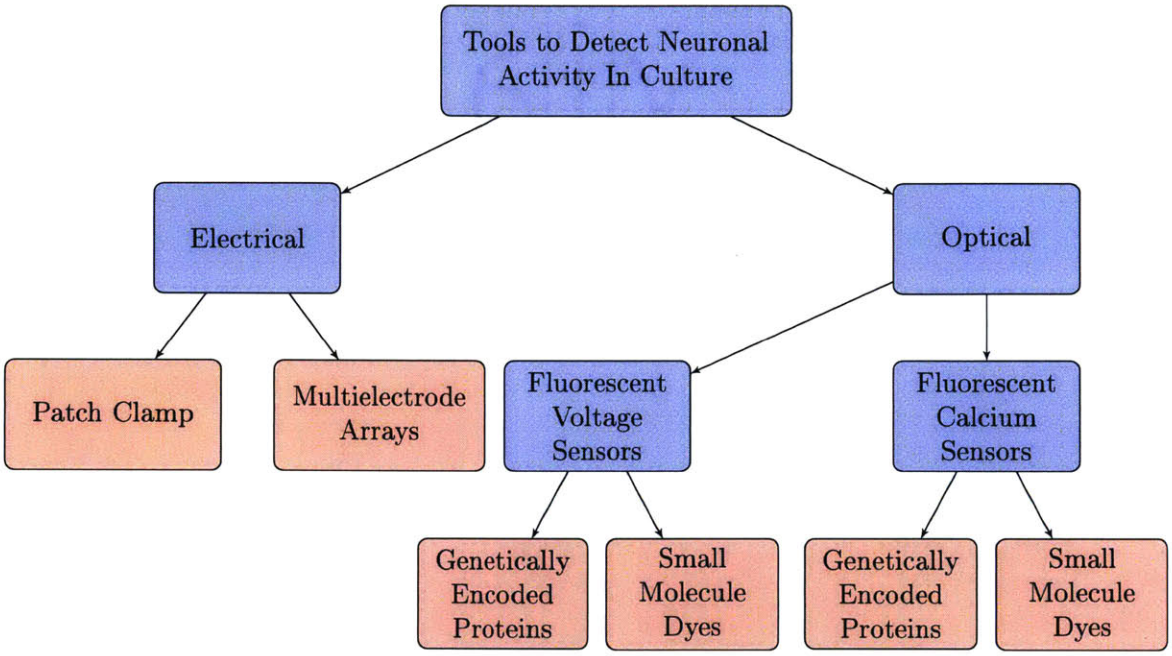

Figure 2-4: The major classes of techniques used to detect neuronal activity in culture are shown above. Blue boxes denote approaches and red boxes represent methods [9] [8] [30].

2.2.1 Electrical methods

Electrical methods place electrodes in close proximity to a region of interest and measure the potential between the sample electrode and a reference electrode [27].

Sharp electrode recordings and patch clamp recordings are common for the study of single cells, both of which utilize a glass micropipette containing a metallic electrode in fluid contact with the intracellular environment of a cell of interest. Sharp-electrode recordings utilize a very sharp tip that can penetrate the membrane and minimally disturb the cellular ionic environment. The patch clamp takes a different approach that brings a micropipette with a large tip (1-3 μm) in suction-sealed contact with the

cell. Individual ion channels can be studied in this modality. Additional suction can be applied to rupture the membrane patch, bringing the electrode inside the pipette in direct electrical contact with the solution inside the cell. The pipette solution gradually dialyzes the intracellular solution over the course of several minutes [28]. The geometries of these setups are shown in Figure 2-5.

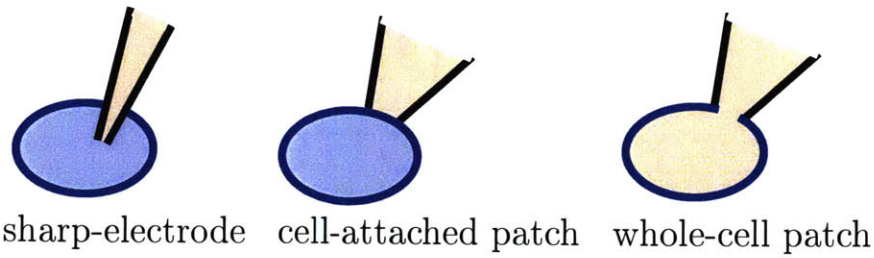

Figure 2-5: The geometry of the pipette and cell for various cellular recording modalities are shown. In each geometry, there is one electrode (commonly Ag/AgCl) inside the micropipette and another ground electrode inside the bath.

Intracellular recordings can be made either in the voltage clamp (VC) mode or the current clamp (IC) mode. In the VC mode, a measurement of the membrane potential is made at some time, compared to a target membrane voltage, and an appropriate amount of current to compensate for the difference is injected into the cell. In this way, the membrane potential is "clamped" to some value. VC experiments allow for the membrane potential to be adjusted independent of the ionic currents, allowing for current-voltage characteristics of the membrane to be studied. Current clamp experiments inject current into the cell and allow the membrane potential to vary. Current clamp experiments allow for the study of the membrane potential in response to electrical stimulation. Together, VC and IC experiments allow for effective characterization of the electrical properties of cells [28].

Recordings from sharp-electrodes and patch clamps provide accurate electrical measurements at very high temporal resolution. They also provide well-localized information about a single cell. However, these methods are very sensitive to physical vibrations and electrical noise. Low-drift micromanipulators and a stable optical setup are needed to minimize physical vibrations and low-noise amplifiers are needed to detect very small currents (on the order of pA). Accordingly, these techniques are

extremely difficult to scale to systems of many neurons [9]. Patch chips, microfluidic devices that break into cells from below through pores, have been used but are limited by their fabrication process–they cannot be specifically targeted to single cells [31].

Multielectrode arrays (MEAs) are devices containing structured arrays of electrodes that are placed in close contact (not intracellularly) to a sample preparation. MEAs are often hundreds to thousands of electrodes in size with micron-scale separation, offering great versatility in the types of experiments that can be run. Simultaneous stimulation/observation through multiple electrodes can be carried out. They provide high-quality spatial resolution of signals due to the nature of the structured array but relating that information to specific cells is challenging, requiring extensive post-processing and inference [9].

2.2.2 Optical methods

Fluorescent voltage sensors or calcium sensors are the most commonly used optical sensors of cellular electrical activity. These sensors are small molecule dyes or genetically encoded proteins that modulate their fluorescent properties as a result of an action potential.

Before describing specific molecular mechanisms of these sensors, several universal limitations of dyes should be noted. First, they suffer from photobleaching, significantly limiting the duration of a recording. For example, the genetically encoded dye ArcLight bleaches on the order of 4.8% per 2 seconds of laser illumination [32]. Second, dyes are often toxic to cells. In addition to intrinsic toxicity, the photobleaching process of all dyes produces free radicals and reactive oxygen species. High power laser excitation also heats up the sample preparation which is particularly problematic for dim dyes requiring stronger excitation [8]. Third, it can be challenging to target the dyes to the appropriate location. The extracellular matrix and plasma membrane are barriers for external staining by a small molecule dye while protein-based sensors require genetic modification.

The workhorse for testing many of the various voltage or calcium imaging indictors is the Human Embryonic Kidney 293 (HEK) cell line. HEK cells are easy to culture,

easy to genetically modify, and more robust than neurons, thus lending themselves well towards screening applications. However, HEK cells are not an ideal model for neurons. Many voltage sensors show significantly higher changes in their fluorescence in HEK cells compared to neurons. For example, ArcLight shows a 35% $\Delta F/F$ change in fluorescence intensity compared to approximately 3-5% $\Delta F/F$ in neurons [32]. Despite this challenge, HEK cells remain a useful organism for testing and engineering sensors. For example, spontaneously spiking HEK cells have been used for electrophysiology-free screening of voltage indicators [33].

Voltage sensors

Voltage-sensitive dyes (VSDs) transduce changes in the membrane potential into changes in the fluorescence emission. There are several significant challenges to this. First, the membrane's electric field is screened by ions in solution. The Debye length in physiological solution is on the order of a nanometer, essentially requiring that voltage-sensors be inside the membrane [8]. This limits the signal as the dye is limited to a two dimensional surface instead of the three dimensional cytosolic volume. The fragility of the membrane to molecular perturbations or intense illumination makes such direct voltage-sensing challenging [8].

There are several commonly used physical mechanisms of voltage sensitivity for dyes. These include methods that use the voltage to alter the dye molecule's shape or position within the membrane resulting in changes in the emission spectra. Related FRET mechanisms utilize voltage-coupled changes in the relative position of the donor/acceptor molecules to modulate the FRET efficiency. An electrochromic or Stark shift mechanism is another significant method to couple the electric field to the fluorescence [8].

The change in voltage during an action potential can be from 80 – 100 mV over a membrane thickness of 5 – 10 nm, leading to a high field change on the order of 10^7 V/m. Many modern small-molecule VSDs are electrochromic dyes that are engineered to respond strongly to the local electric field. These sensors respond quickly to the field since they only rely on charge redistribution instead of conformational

changes [8]. An important examples of a small-molecule electrochromic dye includes the ANNINE-6plus dye [34]. ANNINE-6plus generates a fluorescence contrast of about 30% $\Delta F/F$ for a 100 mV change in mammalian cardiomyocytes [35]. The use of a quantum-confined Stark effect in a quantum dot has also has also been proposed but has yet to be realized [36].

The VoltageFluor family of dyes utilize a different approach to respond to the electric field [37] [38]. These dyes utilize voltage-selective photoinduced electron transfer to quench the excited state of the dye during the resting potential membrane state. Under depolarization, quenching becomes less favorable and the dye fluoresces more brightly. These dyes exhibited a sensitivity of 10% $\Delta F/F$ for a 100 mV depolarization in rat neurons and up to 48% $\Delta F/F$ for a 100 mV depolarization in HEK cells [38].

Genetically-encoded voltage indicators (GEVIs) have the advantage that they can be targeted to specific cells instead of staining every membrane present in a preparation. GEVIs typically have a voltage-sensitive domain (often derived from voltage-gated ion channels) and a fluorescent protein that modulates its fluorescence intensity in response to conformational changes of the voltage-sensitive domain [8] A major family of voltage-imaging proteins are derivatives of the ArcLight protein [39] [32]. ArcLight derivatives have been shown to have a sensitivity of $5\%\Delta F/F$ per 100mV with on/off time constant on the order of 10 ms in neurons. Another novel sensor is ASAP1, exhibiting on/off time constants of approximately 2 ms with 4–5%$\Delta F/F$ change in fluorescence for a single action potential [40].

An important new class of high-performance GEVIs is the Arch family. These voltage sensors are based on Archaerhodopsin 3 (Arch), a microbial light-driven proton pump from *Halorubrum sodomense* [41]. Arch had been used as an optogenetic inhibitor but has been utilized in "reverse" as a voltage sensor. Arch's intrinsic photocurrent has been suppressed in the Arch derivatives QuasAr1 and QuasAr2 [42]. QuasAr1 has a time constant of approximately 50 µs along with a sensitivity of approximately $20\%\Delta F/F$ for an action potential event, putting its time resolution on par with typical electronic methods. QuasAr2 improves the SNR from measurements by exhibiting significantly brighter fluorescence but exhibits a time constant of ap-

proximately 0.4 ms [42]. QuasArs are very dim reporters due to their poor fluorescence quantum yield, requiring their very high high excitation powers. They photobleach quite slowly with time constants on the order of several minutes [42].

Overall, many of the genetically encoded voltage indicators are quite dim and suffer from poor SNR ratios for recordings. Recent work has improved upon many of these limitations from multiple approaches and has produced new families of improved sensors. However, certain limitations remain, including photobleaching, toxicity issues, brightness/SNR challenges, and localization of events at high spatial resolution [43].

Calcium sensors

Calcium sensors use a second messenger approach by detecting the rapid increase (10–100 fold) of intracellular calcium ions that accompanies the action potential [30]. The calcium influx originates from multiple sources including voltage- and ligand-gated ion channels as well as release from storage sites within the cell. Calcium-sensitive dyes can be free in the cytosol which improves the signal. The primary limitation of calcium sensing dyes is in temporal resolution; the timescales of the voltage dynamics are much faster than the time scales at which the changes in intracellular calcium ion concentrations can be detected and transduced into an optical signal. Many common calcium-sensing dyes have on/off times on the order of 100 ms. In addition, subthreshhold events (depolarization events too small to cause an action potential) are difficult to detect via calcium imaging but can be detected via voltage imaging [30].

On a molecular level, calcium-sensitive dyes change their fluorescence emission in response to a binding event of a calcium ion. For small-molecule dyes, the most common approach is through design of a dye with a chelation site for the Ca^{2+} ion. For genetically encoded calcium indicators (GECIs), the most common approach is through engineering fusion proteins containing a calcium binding protein (such as calmodulin) with a fluorescent protein.

The development of early calcium-sensing dyes such as Fura-2 and BAPTA family

dyes were significant early developments. However, for the space of neuroscience applications, they have increasingly replaced by genetically encoded calcium sensors [30]. The GCaMP family of proteins is the most commonly used class of proteins for calcium imaging [44] [45]. The recently engineered GCaMP6f protein shows a fluorescence change of 20–30% $\Delta F/F$ for a single action potential in dissociated rat hippocampal neurons. However, the rise time constants for the dye are on the order of 50 ms and the decay times are approximately 150 ms which is too slow for clear resolution of every action potential [44].

2.2.3 Actuation and all-optical electrophysiology

Sophisticated all-optical electrophysiology experiments require selective stimulation and wide-field observation of a large ensemble of cells. Electrical events need to be detected at millisecond resolution and the cell undergoing each depolarization must be clearly identifiable, a challenge in dense confluent cultures [8]. The stimulation and readout must be optically multiplexable with separate channels for excitation and observation.

Actuation methods form an important part of an all-optical electrophysiology system. There are a variety of approaches for noninvasive actuation of neuronal systems that complement all-optical approaches to electrophysiology [9]. Of particular note are widely used optogenetic methods that use light to selectively neuromodulate cells through introduction of light-activated ion channels into cells. When these ion channels are expressed and exposed to particular wavelengths of light, they open and cause a change in the membrane potential. Both excitatory and inhibitory stimuli can be provided. Recent work in optogenetics has allowed for color multiplexing in stimulation [46]. Specific cells can be targeted through use of a spatial light modulator or a digital micromirror device [47].

Localized heating and chemical stimulation are alternative approaches to optogenetics. The strong water absorption peak in the infrared produces a rapid increase in temperature that causes a transient increase in the membrane capacitance that creates depolarizing currents. A sufficiently strong IR stimulus thus results in the ini-

tiation of an action potential [48]. Magnetic nanoparticles can also be used similarly; radio-frequency fields cause localized heating that results in neuronal stimulation [49]. Chemical stimulants can also modulating the activity of ligand-gated ion channels [50].

All-optical electrophysiology methods are currently limited by the resolution of current voltage/calcium sensing methods. The development of a sensor of cellular electrical activity with high spatiotemporal resolution would enable sophisticated experiments to be performed [8] [3]. A recent protein-based approach to this challenge has been the development of Optopatch, the fusion of QuasAr with a CheRiff, a blue-sensitive optogenetic actuator [42]. However, Optopatch requires extremely high excitation powers, liming the field of view and retains photobleaching limitations of dyes.

Nanomaterials exhibiting non-photobleachable fluorescence may be able to surpass several of these barriers. Fluorescent nanoparticles such as quantum dots or diamond color centers are photostable and can be localized to a high degree of precision using super-resolution microscopy [36] [23]. The nitrogen-vacancy center within diamond is a highly studied crystallographic defect within diamond. Recent work has shown the sensitivity of the nitrogen vacancy center to the electric field as well as the biocompatibility of diamond, suggesting its potential use as an optical indicator of neuronal activity [24] [51].

Chapter 3

The nitrogen vacancy center in diamond and its potential as a voltage sensor

The electronic structure of the NV center is described in Section 3.1. Sensing using the NV center is reviewed in Section 3.2 and biological applications of diamonds containing the NV center are described in Section 3.3. Section 3.4 suggests an approach to investigate voltage sensing with NV centers in nanodiamonds.

3.1 Electronic structure of the NV center

The nitrogen vacancy center is a crystallographic defect in diamond that consists of a substitutional nitrogen atom and an adjacent vacancy in the diamond lattice as shown in Figure 3-1.

The NV center can exist in several different charge states: NV^-, NV^0, and NV^+. The negatively charged NV center NV^- is comprised of six electrons. Using a chemical bonding model, three of those electrons come from the dangling bonds of the carbons adjacent to the vacancy site, two electrons from the nitrogen substitutional impurity, and the sixth electron from an additional donor in the lattice [23]. The loss of one electron from the vacancy yields NV^0 and the loss of a second electron yields

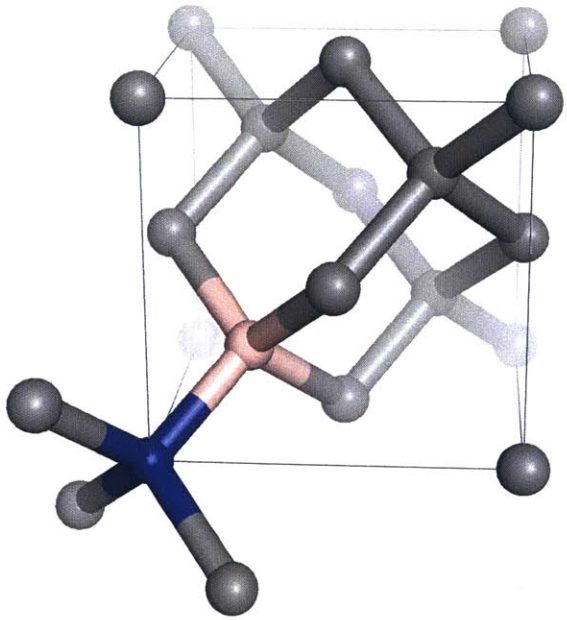

Figure 3-1: Example structure of the NV center within the diamond lattice. The substitutional nitrogen atom is shown in blue and the vacancy is shown in pink.

NV^+. Two out of the six electrons are unpaired; the NV^- center can accordingly be considered as a system of two holes rather than six electrons as an effective spin $S = 1$ system. A simplified energy level diagram of the NV^- center is shown in Figure 3-2 [52] [23].

Diamond has a large bandgap of 5.5 eV that leads to its optical clarity; defects introduce additional states within the bandgap. The electronic structure of the NV^- center consists of a spin triplet ground state $^3A_2$, a spin triplet excited state ^3E and a metastable singlet state with two levels $^1A_1$ and ^1E. The spin triplet ground and excited states are split into sublevels ($m_s = -1, 0, +1$) depending on the electron spins. In the absence of any external field, the $m_s = \pm 1$ spin states are degenerate and show zero-field splittings in the ground and excited states as shown in Figure 3-2 [52] [23] [53]. In the presence of a magnetic field, the degeneracy is lifted and the $m_s = +1$ and $m_s = -1$ states are split by the Zeeman effect. The frequency separation is $2\gamma B$ where γ is the electron gyromagnetic ratio and B is the magnetic field in the direction of the NV axis [52] [23].

The NV^- emission spectrum (shown in Figure 3-3) shows a zero-phonon line

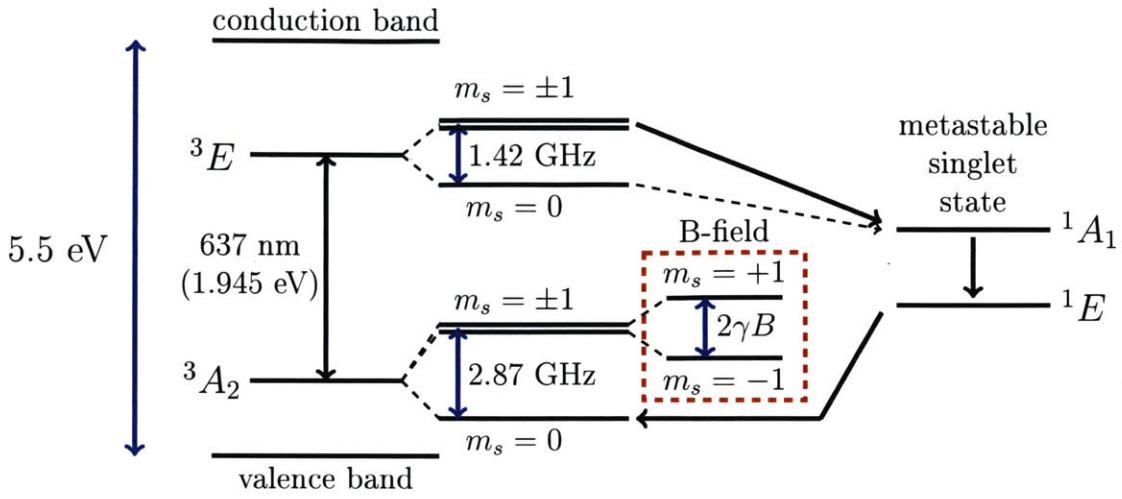

Figure 3-2: Schematic energy level diagram of the electronic structure of the NV^- center. Important transitions are also shown. Based on [52] [23].

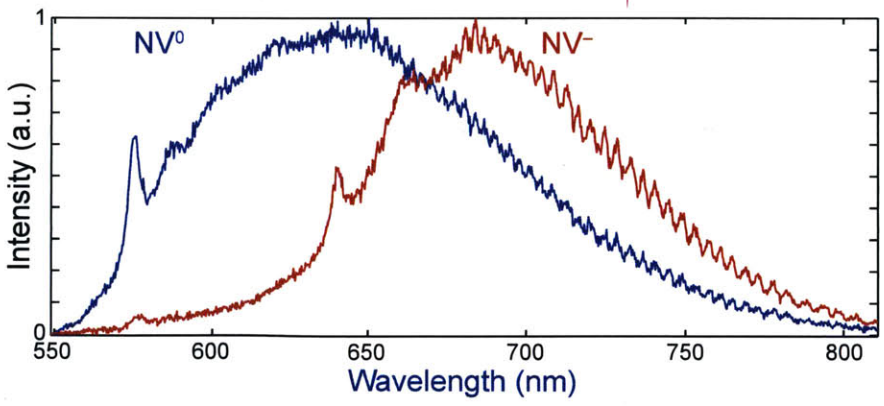

Figure 3-3: NV^- and NV^0 fluorescence emission spectra in high pressure high temperature nanodiamonds at room temperature. Image adopted from [24].

(ZPL) at 637 nm corresponding to transitions between the ^3E excited state and the $^3A_2$ ground state. The emission spectrum also contains a broad phonon sideband from approximately 630 nm to 800 nm. The phonon vibrational modes form a band of states above the $^3A_2$ and ^3E states. Coupling to these modes adds additional transitions that result in the broad phonon sideband [52].

Excitation from the ground state to the excited state of NV^- is spin-conserving [52] [23]. The excited states can decay through two different pathways. The first pathway (spin-conserving) is through a fast radiative transition back to the ground state. The second pathway (spin-nonconserving) is nonradiative decay through the long-lived metastable singlet state $^1A_1$ [23]. An excited state electron in the $m_s = \pm 1$ states has a significantly larger chance of decaying via the nonradiative pathway compared to an excited state electron in the $m_s = 0$ state. The nonradiative decay pathway leads to an optical contrast of approximately 30%. Nonradiative decay through the singlet state repumps the electron to the $m_s = 0$ spin state [52] [23].

The spin state of the NV^- center can be initialized to the $m_s = 0$ state through a long green excitation laser pulse. The application of microwave radiation at resonant frequencies between sublevel transitions can be used to initialize the spin state into the $m_s = +1$ or $m_s = -1$ state [23]. The spin initialization, control, and readout properties of the NV^- center have made it an attractive material for applications in quantum information science and for nanoscale sensing. However, the charge state of the NV^- center is known to be unstable [54] [55] [56]. Certain types of high-intensity laser illumination or diamond surface terminations have been shown to convert NV^- to NV^0 [24]. For spin-based applications in quantum information processing, preservation of the NV^- charge state is essential.

The electronic structure of the NV^0 center is shown in Figure 3-4 and its fluorescence emission spectra is shown in Figure 3-3. The electronic structure of the NV^0 center consists of a spin doublet ground state ^2E and excited state ^2A along with a spin quartet state $^4A_2$ [52] [57] [58]. The NV^0 spectra shows a sharp zero-phonon line at 575 nm with a broad phonon sideband from approximately 580 nm to 750 nm. The differing emission spectrum allows for spectral discernment of the NV center charge

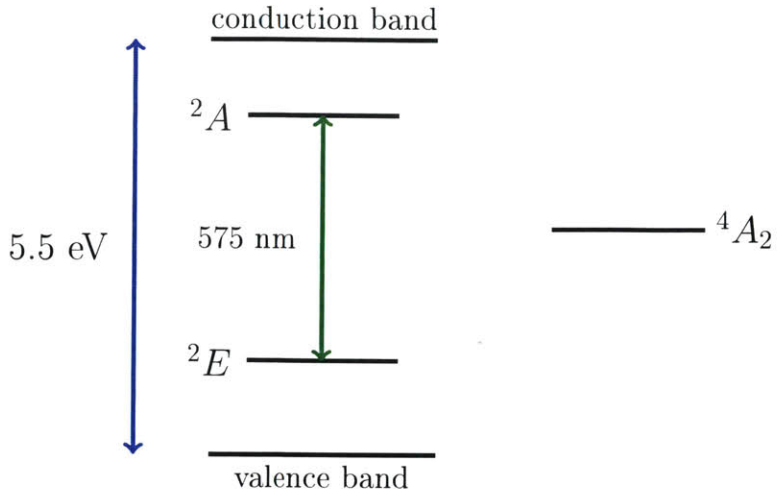

Figure 3-4: Energy level diagram of the electronic structure of the NV^0 center [52].

state.

Much of the attention focused on the NV^0 center has been focused on control and maintenance of the NV^- charge state in bulk diamond [56] [59] [60]. Material engineering and active control systems have been used to control the charge state. For an NV center located near the surface of a bulk diamond crystal, hydrogen-terminated diamond promotes the NV^0 charge state while oxygen-termination promotes NV^- [61]. This has been attributed to band-bending effects caused by the negative electron affinity of the hydrogen termination [24]. Active devices have been fabricated on bulk diamond that apply electric fields that lead to NV charge state switching [59] [60]. In addition, charge-state switching has also been shown in nanodiamonds as well in a model electrochemical cell [24]. Through these methods, it is possible to achieve reversible control of NV^0 to NV^- conversion. In addition, these studies have additionally revealed reversible conversion between NV^0 to the NV^+ charge state, the nonfluorescent dark state [59].

3.2 Sensing using the NV center

The NV^- center has been used for several different sensing systems that take advantage of optical detection of the NV^- spin state. The most widespread application

is for magnetometry [13] [14] [15]. Through optically detected magnetic resonance (ODMR) experiments, microwave radiation through an antenna near the NV^- center is swept through the resonant frequency while observing the fluorescence contrast. When the microwave frequency is on resonance with the ground state $m_s = 0 \rightarrow -1$ transition or the ground state $m_s = 0 \rightarrow +1$ transition, the electron is pumped into the nonzero spin state and accordingly shows optical contrast [13] [14]. The difference between the resonant frequencies of the two transitions corresponds to the magnetic field in the NV axis due to the Zeeman splitting. ODMR with the NV center has been used in widefield imaging with bulk diamond, with nanodiamonds, as well as with scanning probes [23].

In addition to magnetic field sensing, the NV^- center has also been used for sensing of electron spins [62] [63], nuclear spins [64] [65] [66], temperature [67] and charge [68]. Many of these utilize more complex pulse sequences for sensing similar to methods in magnetic resonance imaging [23]. The spin state can also be measured through selective conversion of the $m_s = 0$ state to NV^0, allowing for single-shot readout of the spin state [69].

The NV^- center has also been shown to be sensitive to electric fields through Stark shift and spin-orbit coupling mechanisms [16] [17]. In addition to sensing electric fields directly through these mechanisms, a charge-state conversion scheme between NV^- and NV^0 can be used to measure the local environment of the NV center [59] [24].

Hydroxylated and hydrogenated nanodiamonds have been demonstrated to show reversible control of their charge state through experiments carried out in an electrochemical cell [24]. In Figure 3-5, fluorescence modulation data is shown in response to an applied voltage (adapted from [24]). A 650 nm longpass filter was used in the wide-field image acquisition to select for NV^- fluorescence (as can be seen from Figure 3-3). For hydroxylated NDs, the mechanism is thought to be primarily charge-state switching between NV^- and NV^0 and results from band bending as a result of the electric field from the potential. In the case of hydrogenated NDs, the mechanism is thought to be primarily switching between NV^0 and the nonfluorescent dark state NV^+ and results from modulation of the Fermi level of the ND. Results from the

electrochemical cell studies show that the NV center can serve as an effective sensor for the local potential environment through modulation of the charge state.

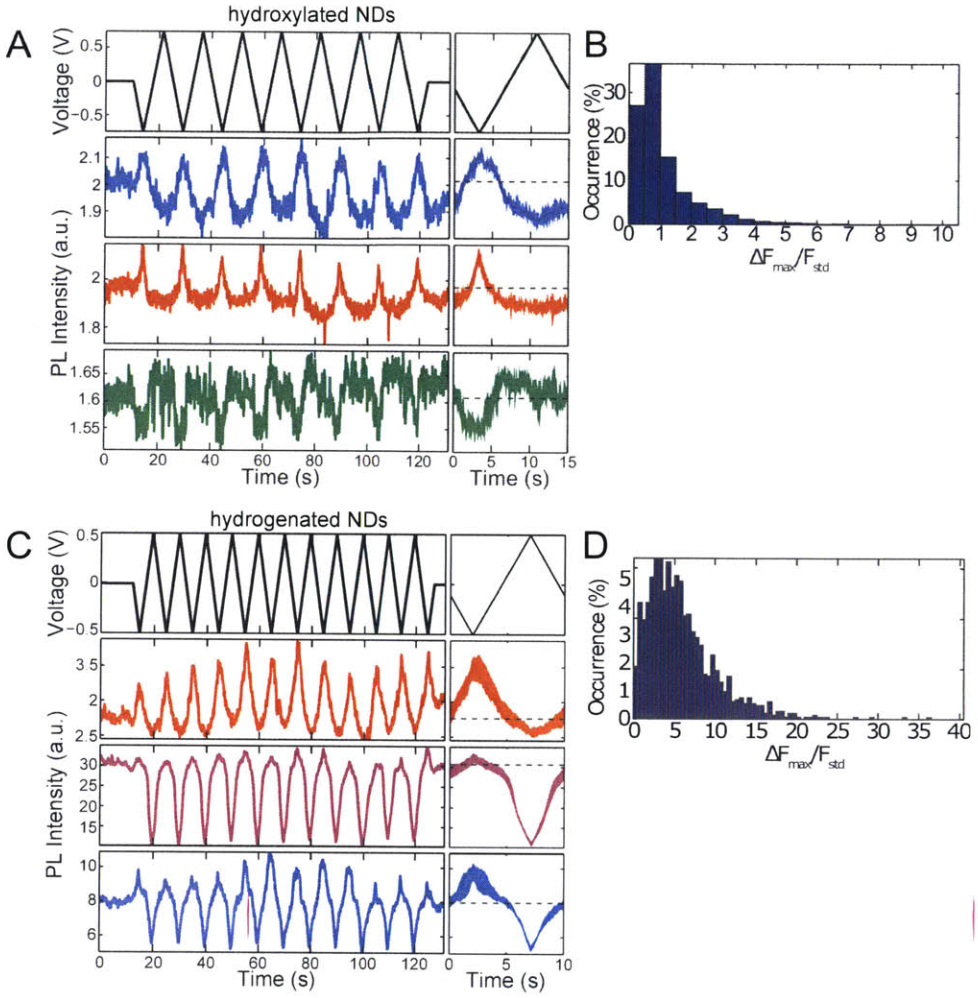

Figure 3-5: **A.** Three representative fluorescence time traces of hydroxylated NDs subject to the voltage trace shown. **B.** Histogram of the average maximal fluorescence contrast percent for hydroxylated NDs. **C.** Representative fluorescence time traces of hydrogenated NDs subject to the voltage trace shown. **D.** Histogram of the average maximal fluorescence contrast percent for hydrogenated NDs. Figure adapted from [24].

The electrochemical cell studies have also shown that NV centers within nanodiamonds are sensitive to small changes in the electric field with high temporal resolution [24]. Figure 3-6A demonstrates individual hydroxylated NDs showing sensitive fluorescence modulation in response to 100 mV square wave pulses. Figure 3-6B demonstrates that a cluster of hydrogenated NDs is sensitive enough to detect 5 ms

duration 100 mV voltage pulses and Figure 3-6C demonstrates that multiple clusters of NDs can be used to detect voltage changes as low as 20 mV [24]. Taken together, these results show that the integrated signal from multiple NV centers are sensitive enough to resolve low amplitude events and are also fast enough to resolve dynamics nearly on the duration of neuronal activity.

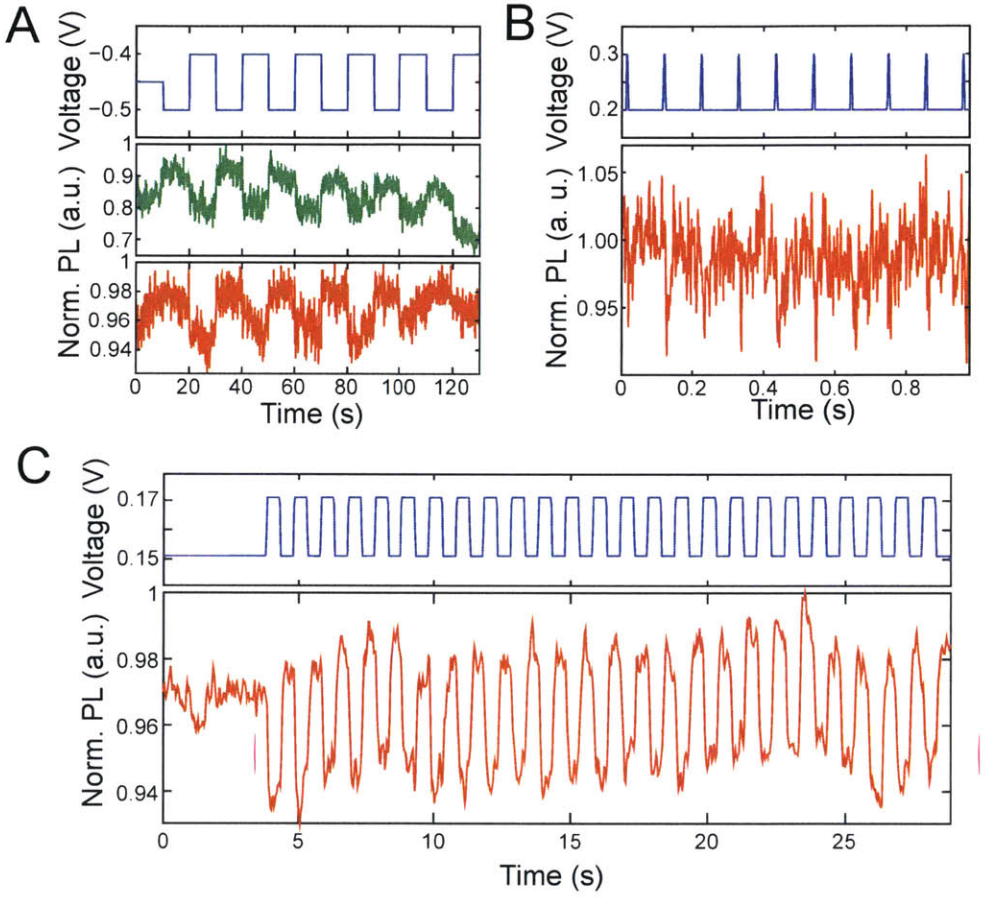

Figure 3-6: **A.** Fluorescence time trace of two hydroxylated NDs in response to 100 mV square wave pulses. **B.** Fluorescence time-trace of a cluster of hydrogenated NDs to 100 mV square wave pulses of duration 5 ms. Figure adopted from [24]. **C.** Fluorescence time traces of multiple clusters of NDs integrated together in response to 20 mV pulses.

3.3 Biological applications of NV centers

NV centers in both bulk diamond and in nanodiamonds have been used for a variety of applications in biosensing and labeling. Diamond is an attractive material for

biological applications as the sp^3 lattice of diamond is chemically nonreactive and biologically inert [70] [51] [71] [72]. Nanodiamonds have been shown to have low cytotoxicity in neurons [51] [71]. In addition, chemical modification of the surface of nanodiamonds enables covalent attachment of biomolecules [23] [73].

The NV center is both bright (emitting more than 10^6 photons/second) and photostable, providing an advantage over small molecule dyes and fluorescent proteins [23]. Photobleaching of emitters is a major limitation of fluorescence microscopy; the absence of photobleaching of the NV center enables longer-duration recordings. The NV center is also compatible with several super-resolutions imaging techniques [74] [75].

Most biological applications of the NV center have focused on the use of the NV center as a photostable tag or on NV^- spin state based sensing. For tagging applications, the NV center has been used for tracking the orientation of nanodiamonds in HeLa cells [76], tracking quiescent cancer stem cells [77], and particle tracking within *Drosophila melanogaster* embryos [78]. NV^- magnetometry has been used to image the magnetic fields of magnetotactic bacteria [79] as well as the magnetic fields of magnetic nanoparticles that selectively labeled cancer cells [80]. Single-cell thermometry has also been performed as well [81].

3.4 Towards voltage sensing with NV centers

The optical properties of the NV^- center suggest its utility as a voltage sensor. The brightness and photostability of the NV center as well as its compatibility with super-resolution methods addresses significant challenges with current tools for optical electrophysiology [23]. Several approaches for NV-based electrophysiology have been proposed.

One approach is to use the NV^- center as a magnetometer to measure the magnetic fields associated with an action potential event [21] [22]. Through physical simulation, neuronal magnetometry using shallow NV centers in bulk diamond has been shown to be viable but has yet to be experimentally realized. A related approach seeks to use

the electric-field dependence of the NV^- center's resonances to detect the changing electric field caused by an action potential [23]. Another approach that has been computationally tested utilizes the optically detected decoherence of an NV center in a diamond scanning probe near the surface of a membrane. The decoherence rate will vary if a nearby ion channel is open or closed [82]. Relaxometry has been experimentally used to locate gadolinium ions labeling phospholipids in an artificial lipid bilayer [83].

In this thesis, charge state switching is targeted as the physical mechanism to transduce local environmental changes to an optical signal for detection of cellular electrical activity. In particular, the time resolution and voltage sensitivity suggest that charge state modulation is a viable viable approach for optical electrophysiology [24]. A characteristic that distinguishes this approach from other proposals for using the NV center for electrophysiology is the absence of microwave control of the NV center. Aqueous solutions absorb microwave radiation and so requiring the delivery of microwave power to NVs located on or near the cell significantly heats the sample, often killing the cells.

A two-part platform was developed to test the utility of the NV center for this optical electrophysiology. The first part was adding the capability to perform electrophysiology experiments to an existing microscope and the second part was optimizing the hydrogen-terminated nanodiamond staining of neurons. Together, these enable experiments where electrical control of cells can be established while changes in the NV fluorescence are detected.

In Chapter 4, the design of the electrophysiology rig is described along with results testing the setup on HEK293 cells. Though the setup was validated on HEK cells, it can immediately be used for experiments on neurons as well. Work on improving the staining efficiency of hydrogen-terminated nanodiamonds on neurons is described in Chapter 5. An existing nanodiamond micellation delivery process [25] was optimized for hydrogen-terminated nanodiamonds. Hydrogenated nanodiamonds showed promising results in an electrochemical cell environment, suggesting the utility of hydrogen-terminated nanodiamonds for sensing action potentials.

Chapter 4

Electrophysiology setup design and measurements

This chapter describes the design of the electrophysiology setup that was built in order to perform electrophysiology experiments on neurons stained with nanodiamonds. A description of the setup is provided in Section 4.1. Electrophysiology experiments on the setup confirming its functionality are described in Section 4.2. A proof of principle experiment of simultaneous electrical/optical recording and future planned electrophysiology experiments are described in Section 4.3.

4.1 Building the electrophysiology setup

4.1.1 Existing microscope setup

The existing optical setup was built by Dr. Sinan Karaveli around a Zeiss Axiovert 200M inverted microscope. Two oil immersion objectives were used: a Zeiss Planapochromat 63x (NA 1.4) objective and a Zeiss Planapochromat 100x (NA 1.4) objective. In addition, a dry Zeiss 63x Neofluar Ph2 (NA 0.75) objective was also used. Wide field fluorescence measurements were carried out with a 300 mW 532 nm continuous wave laser focused to illuminate an region approximately 40 μm in diameter (with the 100x objective). The laser could be attenuated to a desired power using an ND

filter wheel. Fluorescence emission from the sample was collected through the same objective, filtered using either a 562 nm or 650 nm long pass filter, and imaged on a Hamamatsu C9100-13 emCCD camera.

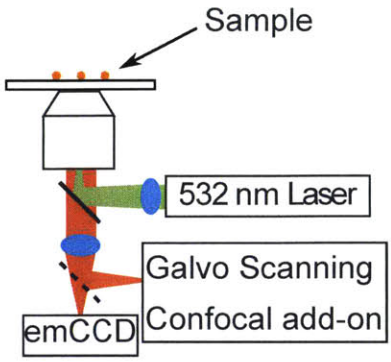

Figure 4-1: A simplified schematic of the microscope is shown. For wide field imaging, a 532 nm laser (for wide field excitation) enters the microscope and is reflected by a dichroic mirror to the sample. The fluorescence is collected and imaged onto an emCCD camera. For confocal imaging, the excitation is provided by the galvanometer scanning confocal add-on. After reflection onto the sample and collection of the emission, the emitted light is spectrally filtered and coupled to a single-mode fiber (not shown). Figure modified and used with permission from Sinan Karaveli.

Confocal measurements were carried out on the same setup. A 532 nm laser that was focused to a diffraction limited spot was scanned in the sample plane using two galvanometer mirrors. The fluorescence was collected through the same path, filtered through a 550 nm long pass filter, and coupled to a single-mode optical fiber connected to either an avalanche photodiode or spectrometer (Princeton Instruments SP2500i with PIXIS 1024B camera). A simplified figure of the input and output of the microscope is shown in Figure 4-1.

4.1.2 Setup of electrophysiology electronics

A Thorlabs movable platform (MP200) was mounted to the right side of the microscope. A right-handed Burleigh micromanipulator (Thorlabs PCS-6300) was mounted to the center of the movable platform using a single screw. The micromanipulator was moved to an appropriate height by adjusting the height of the platform using the movable cuff. The movable cuff was also set up so that the entire movable plat-

form could be rotated outwards from a fixed position (locked by a clamp) near the microscope stage. This allowed for access to the pipette holder mounted on the micromanipulator. The free hinges of the micromanipulator assembly were set so that the micromanipulator did not touch the microscope condenser while also maximizing the angle of approach of the micropipette.

A microelectrode amplifier (Molecular Devices MultiClamp 700B) and digitizer (Molecular Devices DigiData 1550) were set up for use together. Only Channel 1 of the amplifier was used. The primary and secondary output of channel 1 of the amplifier were connected to channel 0 and channel 1 of the analog input to the DigiData 1550, enabling simultaneous voltage and current recordings. The channel 1 headstage was connected to the amplifier and attached to the mounting plate of the micromanipulator. The micromanipulator fine and coarse controls as well as the microscope stage control were placed on an external surface to minimize vibrations.

4.1.3 Pipette holder and micropipette preparation

The pipette holder (Molecular Devices HL-U) interfaced between the micropipettes and the electronics. The longer length (28 mm) holder body was used. The pipette holder was screwed onto the headstage and connected the pipette electrode wire (0.25 mm diameter silver wire) to the headstage electronics through a gold pin. The bottom 1.5 cm of the pipette electrode wire was re-chlorided every 2-3 weeks, forming a suitable silver/silver chloride (Ag/AgCl) electrode. The bath (ground) pellet electrode (In Vivo Metric E205 Ag/AgCl) was connected to the grounding pin and was immersed in the bath of the preparation during measurements.

Pressure control to the setup was applied manually by mouth. A length of silicone tube (Harvard Apparatus 721047, ID 1 mm, OD 2.2 mm) was cut to approximately 1.25 m of length and slipped onto the suction port. A 1000 μL filter pipette tip was inserted into the tube at the other end as the mouthpiece for pressure control and a clip was used to maintain the pressure state.

Patch pipettes were filled with intracellular solution (described in Section 4.2.1) using either a MicroFil 28G or 34G needle (World Precision Instruments). Micropipettes

were filled sufficiently high to ensure contact with the chlorided part of the electrode but not so high that the solution was in contact with the bare silver wire. To secure the patch pipette inside the pipette holder, an appropriately sized rubber washer was used.

Two different sizes of capillary glasses (with internal filaments) were used to pull micropipettes for patch clamping experiments: Sutter Instruments BF150-86-10 ("Thick glass," 1.5 mm OD, 0.86 mm ID, 10 cm length) and Sutter Instruments BF100-50-7.5 ("Thin glass," 1 mm OD, 0.5 mm ID, 7.5 cm length). Patch pipettes were pulled on a Sutter Instruments P-80 pipette puller with a trough filament. The filament position was lopsided, leading to lopsided pipettes that were thinned primarily on one side but were still suitable for patch clamping cells.

Through iterative optimization, programs were obtained to pull patch pipettes. The pipette programs are shown in Table 4.1 and images of the pipettes are shown in Figure 4-2. Figure 4-3 summarizes the build process and provides a cartoon of a patch clamp experiment.

Pipette Type	Heating	Pull	Velocity	Time	Typical tip size	Resistivity
Thick	640	0	12	1	1.7–2.2 μm	7–10 MΩ
Thin	625	0	10	1	1.5 – 2.0 μm	6–10 MΩ

Table 4.1: For each glass pipette capillary, the program used to pull pipettes is shown along with the typical tip size and resistance in solution for an ICS-filled micropipette in a bath of Tyrode's solution.

4.2 Electrophysiology experiments on HEK cells

HEK cells were chosen for testing and validation of the electrophysiology setup. HEK cells are an important workhorse organism for electrophysiology [33]. The setup has been tested and characterized on HEK cells and can be used for neurons without any modifications.

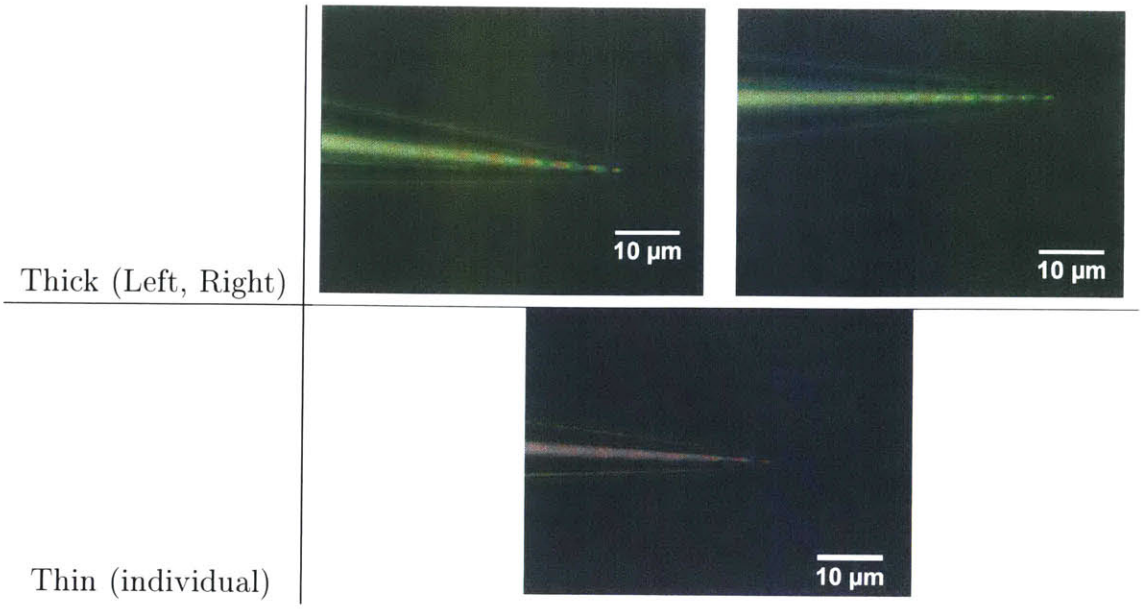

Figure 4-2: Representative images are shown for the left and right pipettes pulled from the thick capilary glass. For the thin glass, only a single pipette is pulled per capilary glass.

4.2.1 Sample preparation

HEK293 cells were prepared in the Boyden laboratory by Dr. Sinan Karaveli; D10 media, Tyrode solution, and intracellular solution (ICS) were provided by the Boyden laboratory. HEK293FT cells (Invitrogen) were cultured at 37°C in D10 medium, consisting of DMEM medium (CellGro) supplemented with 10% fetal bovine serum (Invitrogen), 1% penicillin/streptomycin (CellGro) and 1% sodium pyruvate (Biowhittaker). Cells were plated at 5–10% confluence on glass bottom petri plates that were coated with Matrigel (BD Biosciences). The HEK cells were allowed to grow to 40–60% confluence before electrophysiology experiments were carried out.

Before recordings were taken, the cells were washed three times with Tyrode solution warmed to 37°C that contained 125 mM NaCl, 2 mM KCl, 3 mM $CaCl_2$, 1 mM $MgCl_2$, 10 mM HEPES, and 30 mM glucose at pH 7.3 (NaOH adjusted) and osmolarity 300 mOsm (sucrose adjusted). After the last wash, the cells were bathed in Tyrode solution for the duration of the electrophysiology experiments.

The pipette intracellular solution used to fill the micropipettes contained 125 mM K-Gluconate, 8 mM NaCl, 0.1 mM $CaCl_2$, 0.6 mM $MgCl_2$, 1 mM EGTA, 10 mM

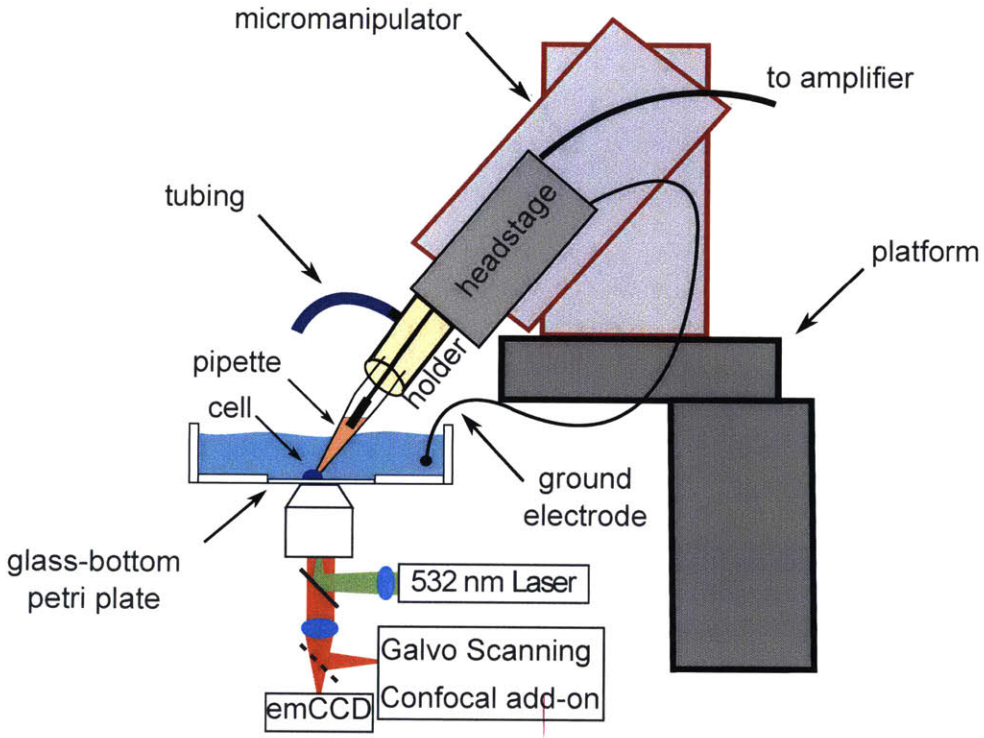

Figure 4-3: The major additions to the setup for electrophysiology are shown. The optics remain unchanged. Cells for electrophysiology are cultured on glass bottom petri plates for imaging. The ground electrode is secured in the bath. The micropipette is partially filled with intracellular solution (ICS) and the chlorided part of the pipette wire electrode is in contact with the ICS. A length of silicone tubing is connected to the pipette holder for buccal pressure manipulation. The pipette holder, headstage, micromanipulator, and mounting platform are connected as shown.

HEPES, 4 mM Mg-ATP, 0.4 mM Na-GTP at pH 7.3 (KOH adjusted) and with osmolarity 300 mOsm (sucrose adjusted).

4.2.2 Patch clamp recordings

Micropipettes were pulled, filled, and secured in the pipette holder. Positive pressure was applied buccally and the pipette was lowered into the sample preparation using the coarse micromanipulator controls. A suitable region of HEK cells was found under 10x magnification (air objective). The micropipette was slowly lowered closer to a cell of interest while observing the preparation using a 40x air objective and the 63x air objective. The 63x air objective, the 63x oil immersion objective, or the 100x oil immersion objective could all be used for patch clamping. For work with NV centers, maximal light collection is sought requiring the use of the oil immersion objectives. Using the appropriate high magnification objective, the pipette was positioned 100 μm above a cell of interest. The electrical response to a square pulse was monitored using the Membrane Test functionality of the Clampex software package. The holding potential was held at -60 mV.

The final approach was controlled using the fine micromanipulator controls. The micropipette was slowly brought into contact with the cell membrane, using the square pulse response to monitor contact. When the micropipette was in contact with the cell membrane (observed as a resistance increase of approximately 0.2 MΩ or instability of the voltage measurements), positive pressure was released and slight negative pressure was applied buccally. After formation of the gigaseal, short pulses (0.5 s) of negative pressure were applied buccally to break into whole-cell recording mode. Entry into whole-cell recording was monitored using Clampex. When cells were confirmed to be patched the whole-cell configuration, standard voltage clamp or current clamp recordings were taken.

Patch clamping was successfully performed using both thick glass and thin glass capillary micropipettes for all three objectives (63x air, 63x oil immersion, 100x oil immersion). Selected data is shown here as validation that the setup is functional.

A current clamp protocol was carried out under the following conditions. A HEK

cell was patch clamped with a micropipette that was was pulled from a thin glass capillary with resistance 8.5 MΩ. The membrane capacitance C_m was 75 pF, the membrane resistance R_m was 60 MΩ, and the access resistance was 1 MΩ. The resting membrane potential was initially measured to be -17 mV. The cell was imaged through the 63x air objective. Figure 4-4 shows a bright-field image of the patch clamped HEK cell as well as the membrane voltage as a result of current injection.

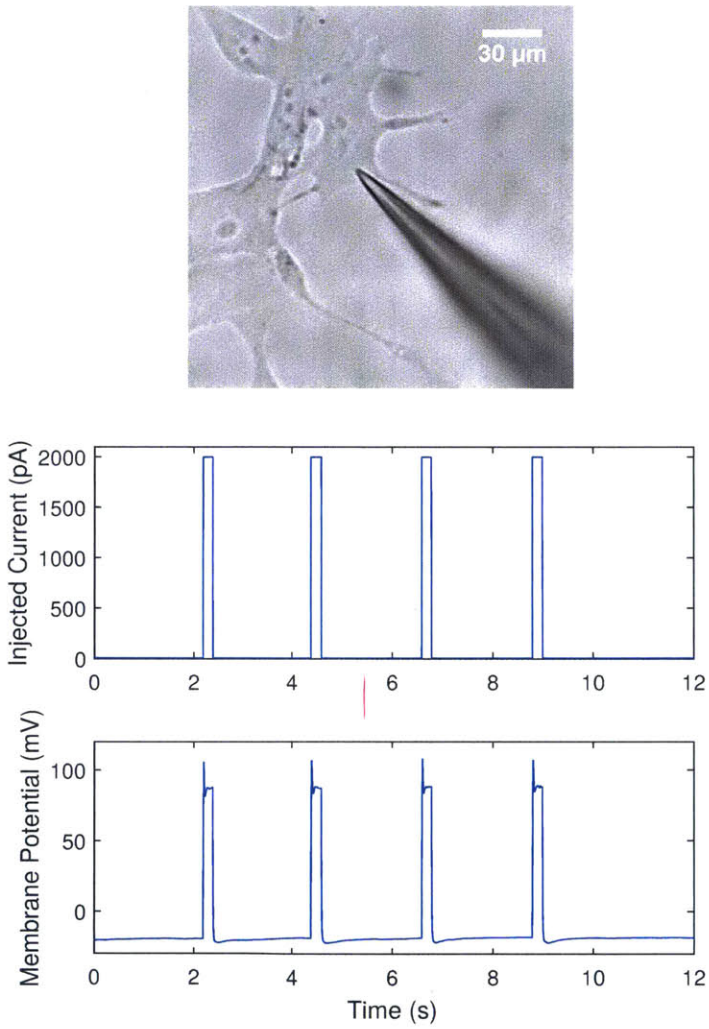

Figure 4-4: **Top.** Bright-field image of patch clamped HEK cell. **Center.** Current clamp experiment protocol for current injection. 2000 pA pulses were injected for 200 ms periodically. **Bottom.** The membrane voltage response to the current injection.

A voltage clamp protocol was also carried out. A thin glass capillary micropipette with resistance 10 MΩ was used to patch clamp a HEK cell. The cell's membrane capacitance was 80 pF, the membrance resistance was 38 MΩ, and the access resistance

was 3 MΩ. The resting membrane potential was initially measured to be -45 mV. Figure 4-5 shows a bright-field image of the patched cell along with voltage clamp data from the cell.

The electrophysiology setup was shown to be functional through using HEK cells for electrophysiology. The optics could be used in parallel with the electrophysiology setup, enabling various forms of spectral characterization in wide-field and confocal modes.

4.3 Model experiment

Once patch clamping HEK cells was possible on the setup, the full data collection and analysis pipeline was developed. To achieve this, electrical recordings needed to be synchronized with the images captured by the emCCD camera in order to synchronize the the membrane potential and fluorescence in time.

To add a realistic signal to a standard HEK cell sample, nanodiamonds were added to the cell preparation. Hydrogen-terminated NDs with NVs (Diamond Nanotechnologies) of average size 18 nm were sonicated for one hour. 10 μL of the solution was added to the center of the preparation into the Tyrode solution bathing the HEK cells. A cell of interest with an NV center cluster close to the cell membrane was selected and patch clamped using the 100x oil immersion objective. Figure 4-6 shows bright-field and fluorescence images of the cell of interest.

The electrical activity of the cell was controlled using a current clamp protocol. Simultaneously, the fluorescence from the NV centers was also collected through a 650 nm long pass filter and imaged into the emCCD camera with exposure time set to 100 ms. During exposures, the camera output 5 V TTL pulses into the DigiData 1550 which recorded the signal alongside the patch clamp results. From this information, the start and end times of each exposure could be determined on the same clock as the membrane potentials. Each frame of the image sequence could be mapped in time to the cell's electrical state.

An analysis code derived from electrochemical NV modulation work [24] was mod-

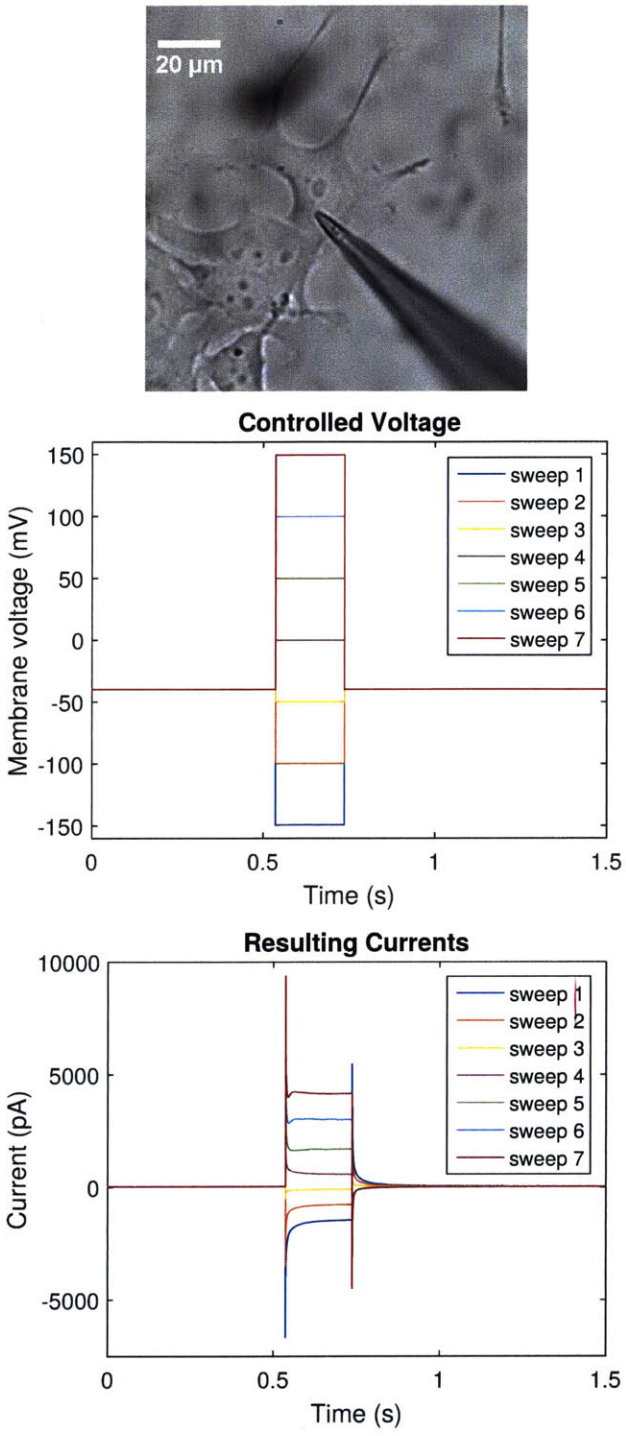

Figure 4-5: **Top.** Bright-field image of patch clamped HEK cell used for voltage clamp experiments. **Center.** The VC experiment stepped from -150 mV to +150 mV in 50 mV steps. The duration of the pulse lasted 200 ms. **Bottom.** The resulting currents needed in order to maintain the membrane potential. Note that no compensation was set on the amplifier, so capacitive transients remain.

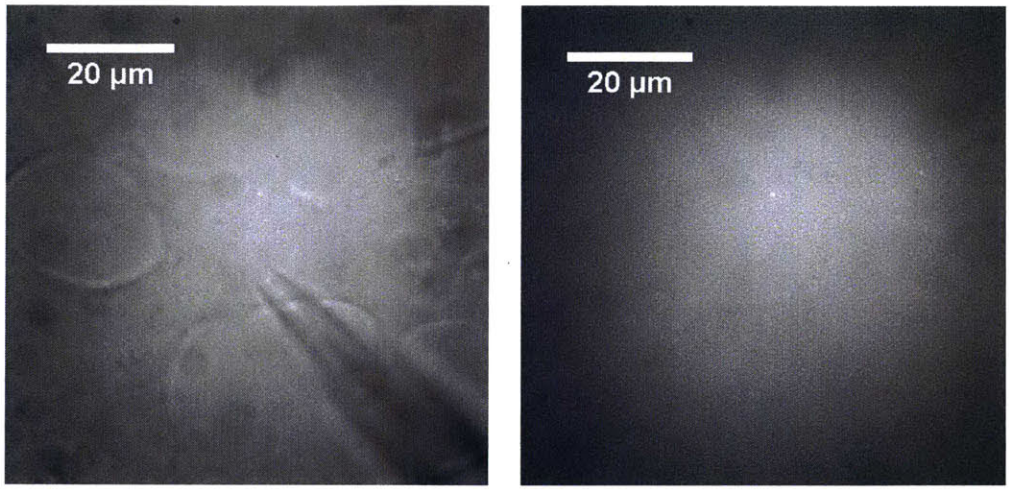

Figure 4-6: **Left.** Fluorescence image with additional bright-field illumination of the patch clamped HEK cell with NVs added to the solution. **Right.** Fluorescence image with no bright-field illumination.

ified by Sinan Karaveli to analyze these data. The results from the first 18 seconds of recording are shown in Figure 4-7 as is the logarithm of the Fourier Transform. The fluorescence intensity does not appear to show any strong correlation to the voltage results in the time domain or in the Fourier domain. For the full duration recording, the fluorescence intensity alone is shown in Figure 4-8. The full trace shows the presence of large changes in the fluorescence intensity on a timescale much slower than the pulses.

The changes in the fluorescence intensity in Figure 4-7 do not resemble the clear changes in Figure 3-6 to low-amplitude variations in the potential. The signal-to-noise ratio of these measurements is low which may obscure any sensing activity. The results in Figure 3-6 were acquired using clusters of nanodiamonds or multiple clusters of nanodiamonds. In these results, only one cluster of nanodiamonds was used. Integration across multiple nanodiamonds may be needed in order to see low-amplitude events. In addition, the nanodiamond was added to solution without any surface chemistry modifications that would aid in targeting it to cells. The nanodiamond may not be on the surface of the membrane, in which case the short 1 nm Debye length of physiological media would screen the electric field.

A possible cause of the large amplitude variations in Figure 4-8 may be due to slow

movement of the sample during the experiment. The seal between the micropipette and cell is maintained by suction, leading to vibrational coupling of the setup to the cell. Large vibrations lead to patch disruption but small vibrations (less than 1 μm) may lead to membrane movement, moving the nanodiamond into and out of the focal plane. To counteract this effect, cells should be patched as far away from the nanodiamond as possible.

The model experiment described confirms that the setup is ready for simultaneous electrical stimulation and optical observation of fluorescence changes. The data acquisition and analysis pipeline is also complete and the setup is ready for experiments on stained cells. In addition, the model experiment also demonstrates the need to label cells effectively with multiple nanodiamonds.

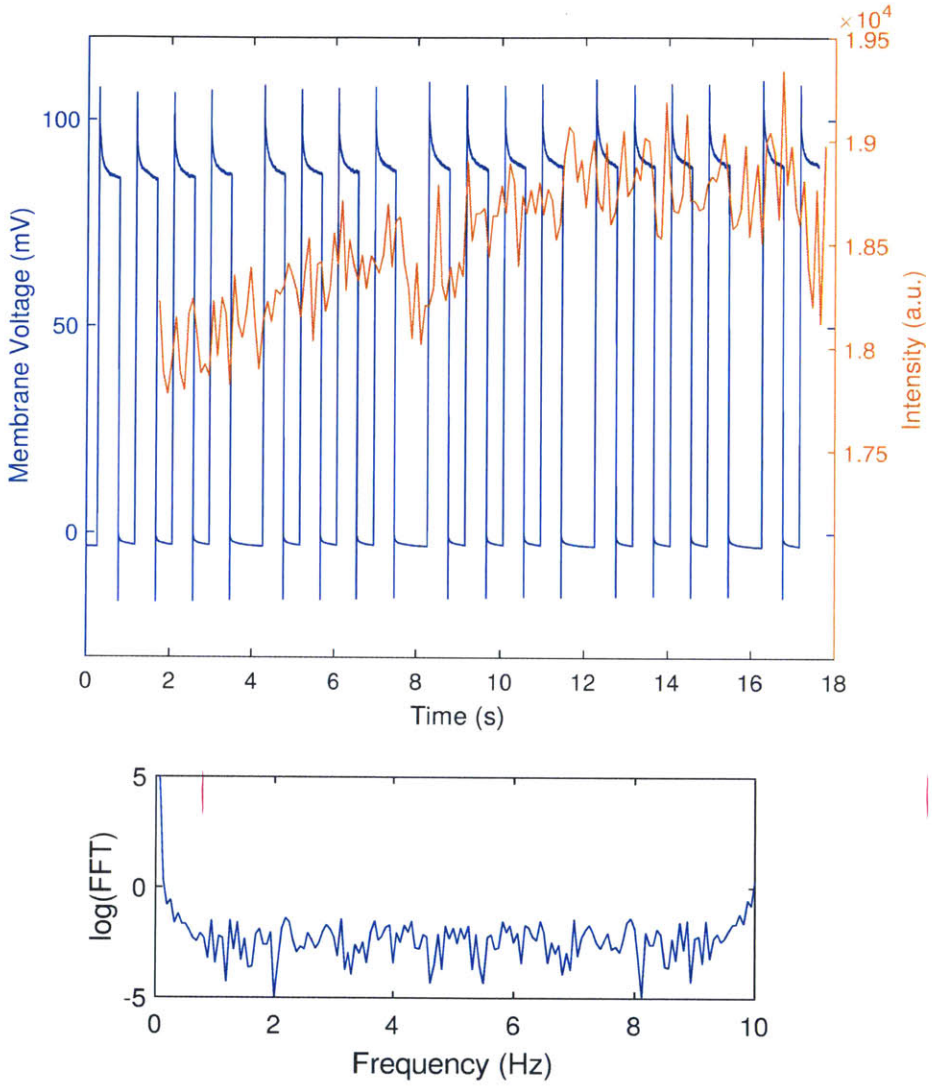

Figure 4-7: **Top.** The membrane voltage and fluorescence intensity from the NV center on the cell are plotted together on the same time axis. **Bottom.** The logarithm of the Fourier Transform for the intensity is shown.

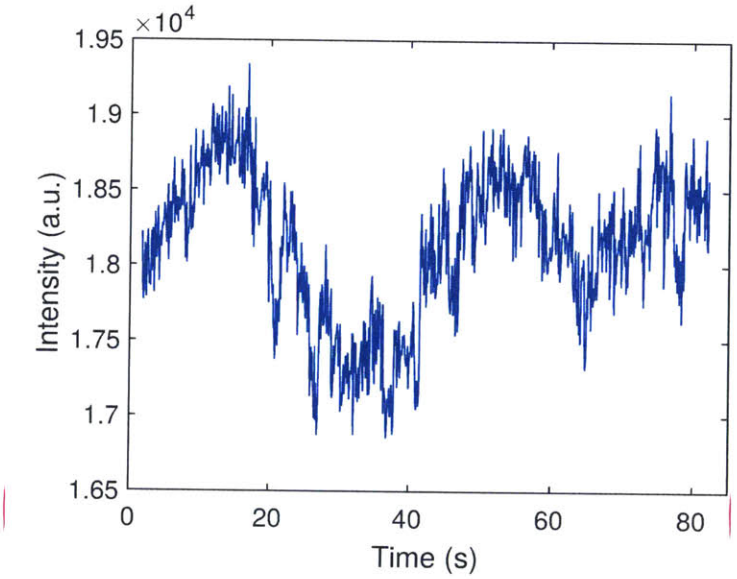

Figure 4-8: The fluorescence intensity for the full duration recording is shown.

Chapter 5

Improved labeling of neurons and HEK293 cells with hydrogenated nanodiamonds

In this chapter, work on optimizing and characterizing the staining of neurons and HEK293 cells with hydrogenated diamonds is discussed. Work on staining HEK cells and neurons with 16 nm nanodiamonds is described in Section 5.1. Optimization of staining neurons with 25 nm nanodiamonds is detailed in Section 5.2.

For optically-detected voltage sensing with nanodiamonds, the nanodiamonds must remain in contact with the cell membrane for long periods of time. Previous attempts at labeling cells with NDs have suffered from internalization [25]. Nanodiamonds have also been shown to rupture intracellular membranes [84]. Recently, a technique to encapsulate nanodiamonds in lipid micelles has been developed that can be used to label neurons with individual nanodiamonds stably for 6-12 hours [25]. The micellation procedure captures nanodiamonds inside a micelle comprised of a lipid component (DOTAP or DMPC) mimicking the phospholipids of biological membranes and a polyethylene glycol polymer conjugated to a phosphoethanolamine (PEG-PE).

Due to voltage dependent charge-state modulation in nanodiamonds [24], hydrogenated nanodiamonds are of great interest for potential sensors of cellular electrical

activity. Previous work on encapsulating nanodiamonds in lipid micelles was not developed for hydrogenated diamonds. Here, we demonstrate the utility of the method for hydrogenated diamonds.

Hydrogen-terminated nanodiamonds were supplied by Diamond Nanotechnologies. The NDs are derived from HPHT diamond and were irradiated and annealed to induce formation of NV centers. The nanodiamond solution concentrations were typically around 1 mg/mL in concentration. Two different sets of nanodiamonds were used: 16 nm hydrogen-terminated NDs in toluene and 25 nm hydrogen-terminated NDs in chloroform. Each sample had a concentration of 1 mg/mL. Toluene samples were stored at room temperature; chloroform samples were stored at 4°C.

5.1 Labeling cells with 16 nm nanodiamonds

5.1.1 Micellation of 16 nm nanodiamonds

The micellation procedure for the 16 nm nanodiamonds was carried out by Or Shemesh based on an existing micellation procedure [25]. The NDs were used without sonication. Three samples of micelles were prepared, each with a different PEG-PE component. 25 μL of the nanodiamond solution was added to 25 μL of DOTAP and 25 μL of a PEG-PE solution (1 mg/mL in chloroform). Several molecular weights of PEG were used: PEG350, PEG2000, and PEG5000 [full name of PEG-PE conjugate: (1,2-dimyristoyl-sn-glycero-3-phosphoethanolamine-N-[methoxy(polyethylene glycol)-[MW])

The solvents were then removed from the solutions using heat and vacuum using a centrifugal vacuum concentrator (CentriVap, Labconco) for one hour at 60°C. 500 μL of distilled water warmed to 80°C was added to each sample. The samples were vortexed and then left in an 80°C water bath for 1 minute. The samples were then horn sonicated for 30 seconds to disperse any additional clusters. After the final mixing, the PEG350-PE and PEG5000-PE samples were non-cloudy and used to label cells.

5.1.2 Staining HEK cells with 16 nm nanodiamond micelles

Staining was first attempted on HEK cells with the PEG350-PE and the PEG5000-PE containing micelles. Micelles were bath sonicated for 30–60 minutes. The volume of Tyrode solution in the well with HEK cells was reduced to 300 μL and 20 μL of the micelle solution was added. After ten minutes, the cells were imaged. Representative images showing staining are shown in Figure 5-1. The staining efficiency was very low using this protocol. Most cells did not show any staining for either set of micelles. The brightness of the spots suggested that the diamonds were not dispersed well during micelle formation and that there were large clusters and aggregates in the micelle solution.

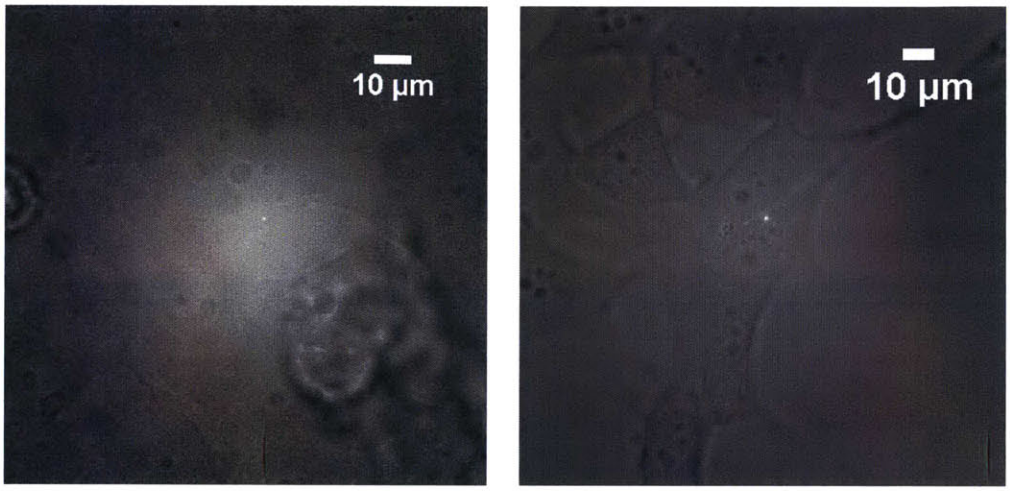

Figure 5-1: **Left.** Representative HEK cell stained with micelles containing PEG350-PE. Sample imaged using 100x oil immersion objective. Mixed bright-field illumination with fluorescence excitation image shown. **Right.** HEK cells stained with PEG5000-PE-containing micelles. Sample imaged with 63x oil immersion objective.

5.1.3 Repeated micellation and characterization

A second group of micelles were prepared. As a result of the aggregation observed in the first set, the nanodiamonds were sonicated before addition of the lipid or polymer components. Two different lipids were also tested: DOTAP and DMPC. The nanodiamond samples were prepared as before along with DOTAP-only and DMPC-only solutions without any PEG-PE components. After following the micellation

protocol as before, the micelles with PEG5000-PE and DOTAP formed a non-cloudy solution, suggesting the presence of viable and disperse micelles. These micelles were used to stain HEK cells with an increased staining duration of 60 minutes at 37°C to maximize staining. The revised process improved staining. Figure 5-2 shows the staining improvement for a representative cell. Using this protocol, some cells had as many as five NDs on their surface across different Z-planes.

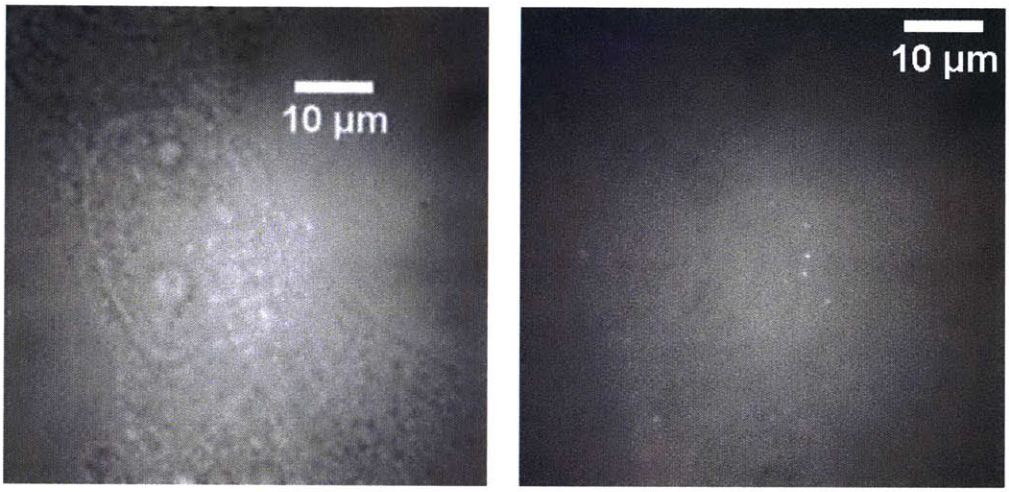

Figure 5-2: HEK cell imaged after staining with improved PEG5000-PE containing micelles. **Left.** Bright-field and laser illumination. **Right.** Fluorescence only.

5.1.4 Staining of neurons with 16 nm nanodiamonds

Live neurons were stained with three micelle samples: DOTAP only, PEG2000-PE and DOTAP, PEG5000-PE and DOTAP.

The protocol for staining neurons was similar to HEK cell staining. The staining duration was for 25 minutes at 37°C. Some cells did show slight staining with nanodiamonds (Figure 5-3). The microscope used was a Leica DMI3000B with a 550 nm long pass filter and a 100x oil immersion objective. For experiments with hydrogen-terminated nanodiamonds, 120 mW of 532 nm laser power was delivered at the sample to approximately a 40 µm diameter circular region. The samples were imaged using a Hamamatsu ORCA-Flash 4.0 scientific CMOS camera.

There were certain spots on the neurons that occasionally blinked brightly. It was

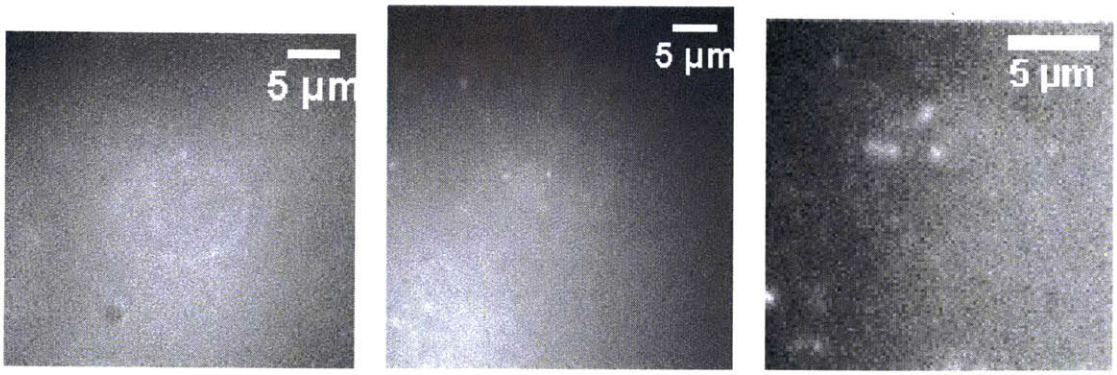

Figure 5-3: Fluorescence images of neurons stained with nanodiamond containing micelles. **Left.** DOTAP-only micelles. **Center.** Micelles with PEG2000-PE and DOTAP. **Right.** Micelles with PEG5000-PE and DOTAP.

thought that these may have been some residue left over from the micellation process. To test this, neurons were stained with the DOTAP-only micelles and fixed using 4% paraformaldehyde. They were imaged on the Zeiss microscope using confocal imaging. Z-stack image sequences were taken and spectra were collected from individual bright spots. From the spectra, nanodiamonds with NV centers could be discerned from other spots. Through scanning several cells, very few (0–2 per cell) NV centers were found. A representative confocal image and spectrum is shown in Figure 5-4. The other bright spots on the cell were also relatively dim, suggesting that the brightness may have come from molecules that photobleached quickly in confocal imaging.

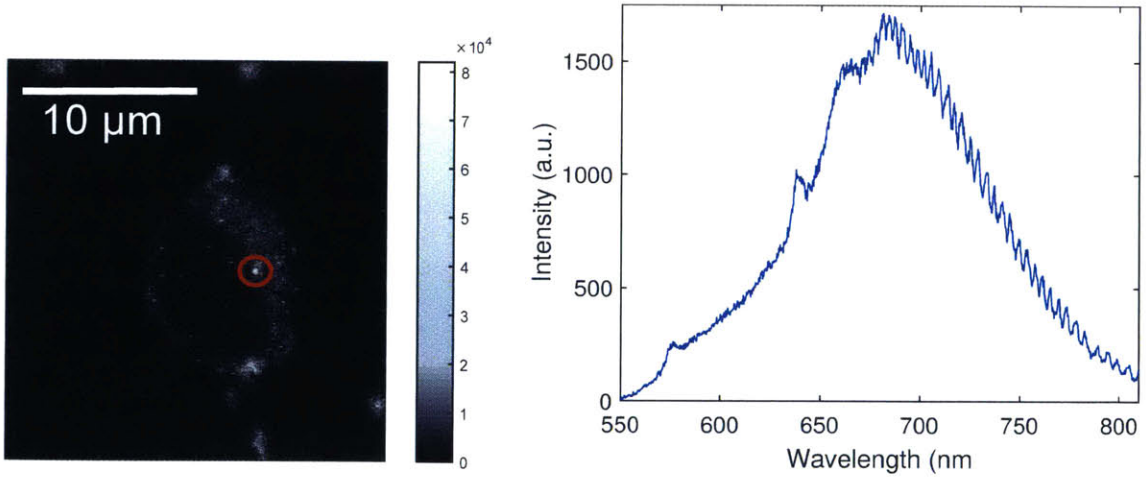

Figure 5-4: Reprentative confocal image and spectrum of an NV center labeling a neuron.

5.2 Labeling neurons with 25 nm nanodiamonds

5.2.1 Characterization of 25 nm hydrogenated nanodiamonds

The 25 nm hydrogenated nanodiamonds from Diamond Nanotechnologies were sonicated for two hours before being dropcast onto a coverslip and imaged using the Zeiss microscope. Wide-field, confocal, and selected spectra are shown in Figure 5-5. Examining additional spectra indicates that many NDs have significant NV^0 character in their emission spectrum.

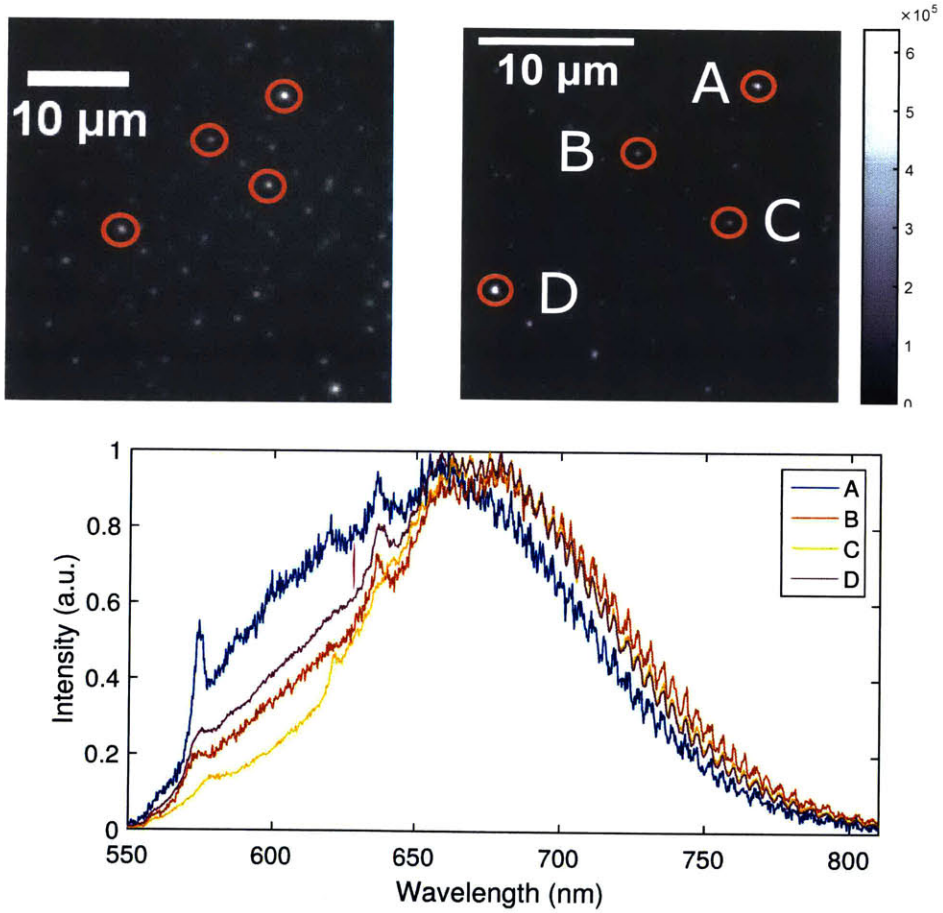

Figure 5-5: **Upper Left.** A wide-field image of the nanodiamonds is shown. Laser excitation power was 70 mW and the sample was imaged through the 100x oil immersion objective. Four NVs are highlighted in red. **Upper Right.** A confocal image of the nanodiamonds is shown. The color bar is the number of counts from the APD and the x-y axes are in microns. The four spots from the wide-field image are highlighted in this figure. Confocal scans were taken with 200 μW of power with a dwell time of 2 ms. **Bottom.** Spectra from the labeled points.

5.2.2 Micellation and optimization of staining conditions

Micellation was carried out by Ishan Gupta. The 25 nm hydrogenated NDs were tip sonicated. Three types of micelles were made with two concentrations each: DOTAP (lipid) only, DOTAP and PEG350-PE, and PEG350-PE only. For each of the six sample preparations, 25 μL of the ND solution was used. For the more concentrated solutions, 50 μL of DOTAP or 50 μL of PEG350 or 25 μL of both DOTAP and PEG350 were added. For the less concentrated solutions, 5 μL of DOTAP or PEG350 or 2.5 μL of DOTAP and PEG350 were added to the ND solution. Chloroform was added to bring the total volume to 500 μL.

The solvents were removed from the solutions using a centrifugal vacuum concentrator for two hours at 60° C until all the chloroform had evaporated. The remaining residue was heated in a water bath at 80° C for five minutes before 500 μL of 80° C Tyrode solution was added. Upon mixing, micelles formed quickly and the solutions became less cloudy. The micelles were tip-sonicated again to ensure adequate mixing and were stored at 4°C.

All neurons used were from C57 mice (Jackson Labs) and were prepared by Or Shemesh based on a protocol from [85]. Hippocampal regions of postnatal day 0 or day 1 mice were isolated and digested with trypsin. They were then treated with Hanks solution supplemented with 10-20% fetal bovine serum and trypsin inhibitor (Sigma). The tissue was then manually dissociated and centrifuged at 1000 rpm at 4°C for ten minutes. Dissociated neurons were plated on glass coverslips coated in Matrigel. The plating medium consists of Neurobasal Medium supplemented with B27 (Invitrogen) and glutamine.

Micelles were removed from 4°C storage and were examined. The solutions of PEG350-PE with DOTAP micelles along with the DOTAP-only micelles appeared cloudy in color, suggesting aggregation that would make labeling difficult. The solutions of PEG350-only micelles were much clearer, so those micelles were used. Two types of PEG350 micelles were used, those with PEG350 (1X) and those with less PEG350 (10X).

5.2.3 Imaging of live neurons

For each micelle type, the staining conditions were varied. Neurons were either stained in plating medium or in Tyrode solution. For the samples with the 10X micelle solution, there was very little staining. Excess diamond was visible but much of it was free in solution. For the samples with 1X micelle solution, staining worked more efficiently. Figure 5-6 shows some of the results from characterizing the staining efficiency.

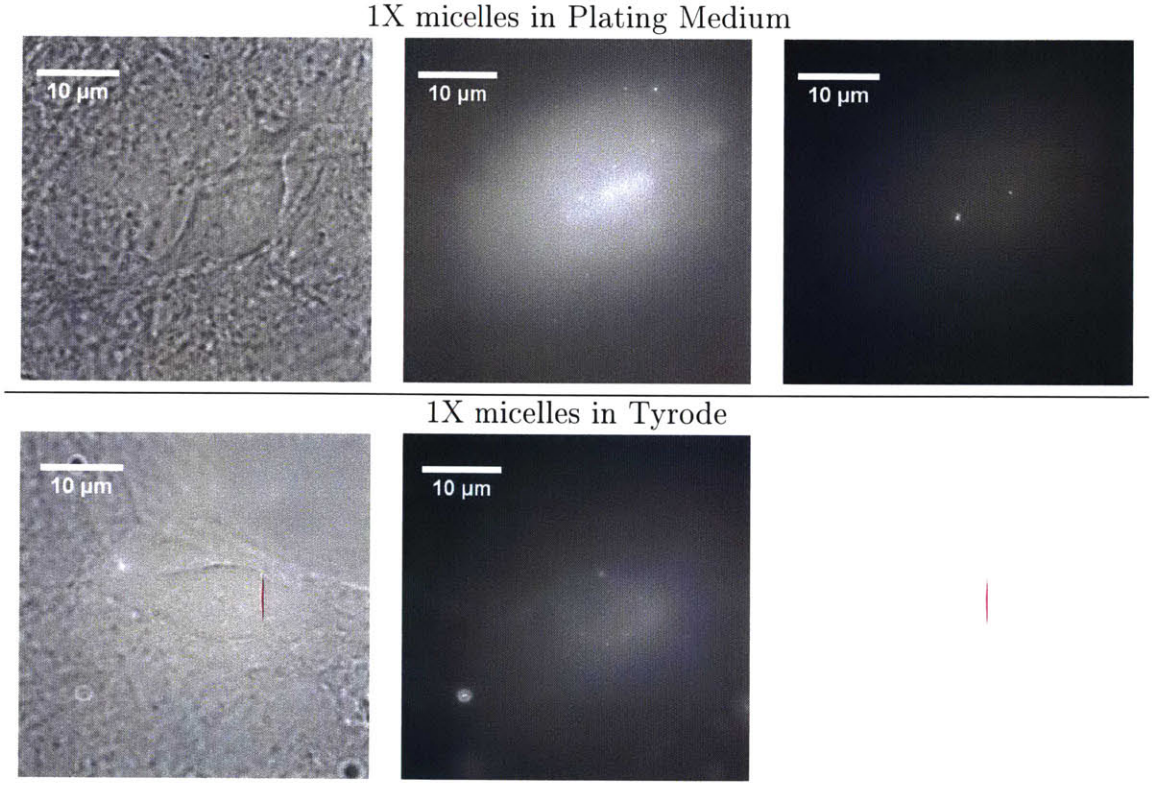

Figure 5-6: The staining efficiency is shown for representative cells for the 1X micelles in Plating Medium and in Tyrode solution. In plating medium, there are nine bright spots on various z-planes for that cell (two shown). For the staining carried out in Tyrode solution, there are five bright spots on several z-planes for the cell. Overall, staining in plating medium led to more NVs per cell.

The staining protocol for the 25 nm hydrogenated diamonds is repeatable. A limitation is that the micelles appear to slowly degrade in storage at 4°C. As the sample became older, the staining efficiency went down. Aggregation is likely the cause of this, so sonication may help with this issue. Six weeks after the last successful

staining with the 1X micelles, staining was attempted again. Figure 5-7 provides an example of a cell micellated under the same conditions but exhibits much lower micellation efficiency.

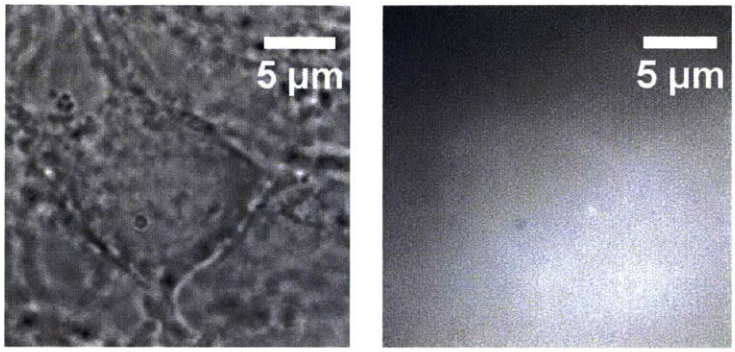

Figure 5-7: Wide-field and fluorescence images of a cell stained using the optimal protocol that exhibited poor staining. This image was taken six weeks after the micelles were prepared.

Imaging of fixed neurons

To better understand the micellation process of these diamonds on the neurons, neurons were stained with PEG350-PE only micelles with 25 nm NDs as described previously and then fixed with 4% paraformaldehyde. The coverglass within the well of the petri plate was flipped over in order to reduce the thickness of the sample and was imaged using the 100x oil immersion lens of the Zeiss microscope. Successive Z-stacks of cells were taken to count the total number of nanodiamonds on a single cell.

Figure 5-8 shows a bright-field and a Z-projection image of a Z-stack taken on a stained neuron. The projection image selects the brightest pixel across all Z-levels for each location. Ten bright emitters are directly on the cell of interest, with additional emitters visible on the other cells. The original Z-stack was 8 images with 1 μm separation between images. Through examining multiple cells, it was found that the staining density was between 4–12 nanodiamonds per cell for cells that were stained.

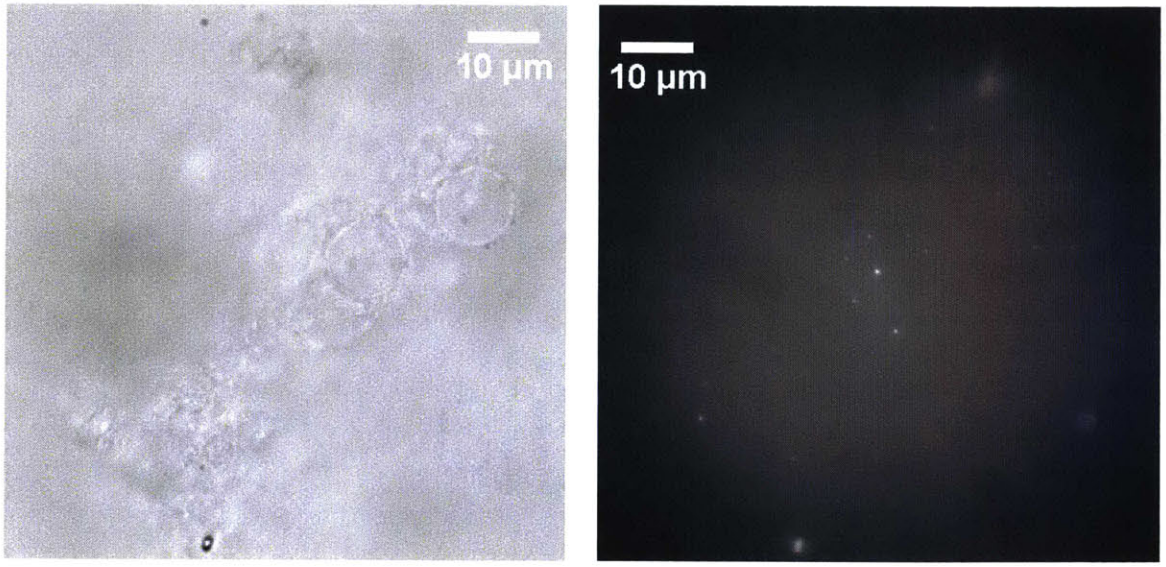

Figure 5-8: Bright-field and fluorescence images (Z-projection) are shown for a stained neuron.

5.3 Summary of micellation experiments

Micellation was performed on two different sizes of hydrogen-terminated nanodiamonds. For the 16 nm diamonds, micellation of HEK293 cells was slightly improved. It was also shown that the 16 nm could be used to label neurons. However, the 16 nm diamonds were challenging to work with and showed relatively low labeling efficiency. In particular, they showed significantly more aggregation than the 25 nm diamonds, limiting the number of separate spots that could be imaged within one focal plane.

The 25 nm diamonds were micellated more effectively and the process of staining neurons was optimized. Through both wide-field and confocal fluorescence microscopy, more effective staining of neurons with nanodiamonds was shown.

The original protocol was optimized for 40 nm and 100 nm hydroxylated nanodiamonds. It is plausible that the relative ratios of lipid and PEG and nanodiamonds may need to be varied beyond the range that has been tested so far to improve the micellation further.

Chapter 6

Conclusions and future outlook

The work in this thesis describes the development of a platform for the study of the fluorescence from NV centers for the detection of cellular electrical activity. This work draws heavily upon recent results demonstrating the sensitivity of hydrogenated nanodiamonds to the electrochemical potential [24] as well as to the development of methods for staining neurons with nanodiamonds [25].

The setup integrating an electrophysiology setup with the home built optical microscope enables spectral characterization of NV centers in nanodiamonds. Since the process of patch clamping relies primarily on an electrical nanodiamondsreadout, it is possible to characterize nanodiamonds that label a cell through confocal methods. Ultimately, the NV center is sought for wide-field imaging of ensembles of neurons, and the optical setup is suitable for working towards this goal.

Nanodiamond surface chemistry is another active area of research. The mechanism for hydrogenated nanodiamond sensitivity to the electrochemical potential is thought to be a result of shifting the Fermi level of the nanodiamond. Functionalization of the nanodiamond surface may enhance this effect in solution environments. For example, functionalization with a conductive polymer may improve charge transfer between the NV center and the environment thus enhancing contrast. The Fermi level may also be tuned, bringing the voltage region of highest contrast closer to that of the neuronal action potential. In addition to the NV center, many diamond color centers have been discovered. Many of these have yet to be characterized for sensitivity to the

electric field or electrochemical potential, opening up other avenues of exploration.

Using HEK cells with the electrophysiology setup enables rapid study of different nanodiamond fabrication processes. Although there are challenges in translating results from HEK cells to neurons, characterization using HEK cells is still a useful tool for neuroscience.

Through the work presented in this thesis, the dependence of NV centers in hydrogenated nanodiamonds is ready to be evaluated with the long term objective of developing a new class of stable optical sensors for cellular electrical activity.

Bibliography

[1] Sebastian Seung. *Connectome: how the brain's wiring makes us who we are.* Mariner Books, Houghton Mifflin Harcourt, Boston, 2013.

[2] A. P. Alivisatos, M. Chun, G. M. Church, K. Deisseroth, J. P. Donoghue, R. J. Greenspan, P. L. McEuen, M. L. Roukes, T. J. Sejnowski, P. S. Weiss, and R. Yuste. Neuroscience. the brain activity map. *Science*, 339(6125):1284–5, 2013.

[3] Rafael Yuste. From the neuron doctrine to neural networks. *Nat Rev Neurosci*, 16(8):487–497, 2015.

[4] M. Helmstaedter, K. L. Briggman, S. C. Turaga, V. Jain, H. S. Seung, and W. Denk. Connectomic reconstruction of the inner plexiform layer in the mouse retina. *Nature*, 500(7461):168–74, 2013.

[5] K. J. Hayworth, C. S. Xu, Z. Lu, G. W. Knott, R. D. Fetter, J. C. Tapia, J. W. Lichtman, and H. F. Hess. Ultrastructurally smooth thick partitioning and volume stitching for large-scale connectomics. *Nat Methods*, 12(4):319–22, 2015.

[6] Melike Lakadamyali, Hazen Babcock, Mark Bates, Xiaowei Zhuang, and Jeff Lichtman. 3d multicolor super-resolution imaging offers improved accuracy in neuron tracing. *PLoS ONE*, 7(1):e30826, 2012.

[7] Shlomo Tsuriel, Sagi Gudes, Ryan W. Draft, Alexander M. Binshtok, and Jeff W. Lichtman. Multispectral labeling technique to map many neighboring axonal projections in the same tissue. *Nat Meth*, 12(6):547–552, 2015.

[8] Darcy S. Peterka, Hiroto Takahashi, and Rafael Yuste. Imaging voltage in neurons. *Neuron*, 69(1):9–21.

[9] Adam Henry Marblestone, Bradley M Zamft, Yael G Maguire, Mikhail G Shapiro, Thaddeus R Cybulski, Joshua I Glaser, Dario Amodei, P. Benjamin Stranges, Reza Kalhor, David A Dalrymple, Dongjin Seo, Elad Alon, Michel M Maharbiz, Jose M Carmena, Jan M Rabaey, Edward S Boyden, George M Church, and Konrad P Kording. Physical principles for scalable neural recording. *Frontiers in Computational Neuroscience*, 7, 2013.

[10] M. V. Gurudev Dutt, L. Childress, L. Jiang, E. Togan, J. Maze, F. Jelezko, A. S. Zibrov, P. R. Hemmer, and M. D. Lukin. Quantum register based on individual electronic and nuclear spin qubits in diamond. *Science*, 316(5829):1312–1316, 2007.

[11] H. Bernien, B. Hensen, W. Pfaff, G. Koolstra, M. S. Blok, L. Robledo, T. H. Taminiau, M. Markham, D. J. Twitchen, L. Childress, and R. Hanson. Heralded entanglement between solid-state qubits separated by three metres. *Nature*, 497(7447):86–90, 2013.

[12] E. Togan, Y. Chu, A. S. Trifonov, L. Jiang, J. Maze, L. Childress, M. V. G. Dutt, A. S. Sorensen, P. R. Hemmer, A. S. Zibrov, and M. D. Lukin. Quantum entanglement between an optical photon and a solid-state spin qubit. *Nature*, 466(7307):730–734, 2010.

[13] Gopalakrishnan Balasubramanian, I. Y. Chan, Roman Kolesov, Mohannad Al-Hmoud, Julia Tisler, Chang Shin, Changdong Kim, Aleksander Wojcik, Philip R. Hemmer, Anke Krueger, Tobias Hanke, Alfred Leitenstorfer, Rudolf Bratschitsch, Fedor Jelezko, and Jorg Wrachtrup. Nanoscale imaging magnetometry with diamond spins under ambient conditions. *Nature*, 455(7213):648–651, 2008.

[14] J. M. Taylor, P. Cappellaro, L. Childress, L. Jiang, D. Budker, P. R. Hemmer, A. Yacoby, R. Walsworth, and M. D. Lukin. High-sensitivity diamond magnetometer with nanoscale resolution. *Nat Phys*, 4(10):810–816, 2008.

[15] J. R. Maze, P. L. Stanwix, J. S. Hodges, S. Hong, J. M. Taylor, P. Cappellaro, L. Jiang, M. V. Gurudev Dutt, E. Togan, A. S. Zibrov, A. Yacoby, R. L. Walsworth, and M. D. Lukin. Nanoscale magnetic sensing with an individual electronic spin in diamond. *Nature*, 455(7213):644–647, 2008.

[16] Eric Van Oort and Max Glasbeek. Electric-field-induced modulation of spin echoes of n-v centers in diamond. *Chemical Physics Letters*, 168(6):529–532, 1990.

[17] F. Dolde, H. Fedder, M. W. Doherty, T. Nobauer, F. Rempp, G. Balasubramanian, T. Wolf, F. Reinhard, L. C. L. Hollenberg, F. Jelezko, and J. Wrachtrup. Electric-field sensing using single diamond spins. *Nat Phys*, 7(6):459–463, 2011.

[18] V. M. Acosta, E. Bauch, M. P. Ledbetter, A. Waxman, L. S. Bouchard, and D. Budker. Temperature dependence of the nitrogen-vacancy magnetic resonance in diamond. *Physical Review Letters*, 104(7):070801, 2010.

[19] Ritwik Kumar Roy and Kwang-Ryeol Lee. Biomedical applications of diamond-like carbon coatings: A review. *Journal of Biomedical Materials Research Part B: Applied Biomaterials*, 83B(1):72–84, 2007.

[20] Tzu-Chia Hsu, Kuang-Kai Liu, Huan-Cheng Chang, Eric Hwang, and Jui-I. Chao. Labeling of neuronal differentiation and neuron cells with biocompatible fluorescent nanodiamonds. *Sci. Rep.*, 4, 2014.

[21] L. T. Hall, G. C. G. Beart, E. A. Thomas, D. A. Simpson, L. P. McGuinness, J. H. Cole, J. H. Manton, R. E. Scholten, F. Jelezko, Jörg Wrachtrup, S. Petrou, and L. C. L. Hollenberg. High spatial and temporal resolution wide-field imaging of neuron activity using quantum nv-diamond. *Scientific Reports*, 2:401, 2012.

[22] A. Cooper, E. Magesan, H. N. Yum, and P. Cappellaro. Time-resolved magnetic sensing with electronic spins in diamond. *Nat Commun*, 5, 2014.

[23] Romana Schirhagl, Kevin Chang, Michael Loretz, and Christian L. Degen. Nitrogen-vacancy centers in diamond: Nanoscale sensors for physics and biology. *Annual Review of Physical Chemistry*, 65(1):83–105, 2014.

[24] Sinan Karaveli, Ophir Gaathon, Abraham Wolcott, Reyu Sakakibara, Or A. Shemesh, Darcy S. Peterka, Edward S. Boyden, Jonathan S. Owen, Rafael Yuste, and Dirk Englund. Modulation of nitrogen vacancy charge state and fluorescence in nanodiamonds using electrochemical potential. Unpublished manuscript.

[25] Or Shemesh, Ishan Gupta, Asmamaw Wassie, Ophir Gaathon, Daniel M. Alarcon, Christopher Foy, Sinan Karaveli, Jae-Byum Chang, D.S. Yun, Suhasa Kodandaramaiah, Ian Wickersham, Abraham Wolcott, Dirk Englund, and Edward S. Boyden. Membrane-targeted monodisperse nitrogen vacancy nanodiamonds for uniform labeling of neurons. Unpublished manuscript.

[26] John Gabrieli. 9.00 introduction to psychology, spring 2011. (Massachusetts Institute of Technology: MIT OpenCouseWare), `http://ocw.mit.edu` (Accessed August 5, 2015). License: Creative Commons BY-NC-SA.

[27] Thomas Fischer Weiss. *Cellular biophysics.* MIT Press, Cambridge, Mass., 1996.

[28] Areles Molleman. *Patch clamping : an introductory guide to patch clamp electrophysiology.* J. Wiley, New York, 2003.

[29] Nicholas T. Carnevale and Michael L. Hines. *The NEURON book.* Cambridge University Press, Cambridge ; New York, 2005.

[30] Christine Grienberger and Arthur Konnerth. Imaging calcium in neurons. *Neuron*, 73(5):862–885, 2012.

[31] John Dunlop, Mark Bowlby, Ravikumar Peri, Dmytro Vasilyev, and Robert Arias. High-throughput electrophysiology: an emerging paradigm for ion-channel screening and physiology. *Nat Rev Drug Discov*, 7(4):358–368, 2008.

[32] Lei Jin, Zhou Han, Jelena Platisa, Julian R A. Wooltorton, Lawrence B Cohen, and Vincent A Pieribone. Single action potentials and subthreshold electrical events imaged in neurons with a fluorescent protein voltage probe. *Neuron*, 75(5):779–785, 2012.

[33] Jeehae Park, Christopher A. Werley, Veena Venkatachalam, Joel M. Kralj, Sulayman D. Dib-Hajj, Stephen G. Waxman, and Adam E. Cohen. Screening fluorescent voltage indicators with spontaneously spiking hek cells. *PLoS ONE*, 8(12):e85221, 2013.

[34] Peter Fromherz, Gerd HÃijbener, Bernd Kuhn, and MarlonJ Hinner. Annine-6plus, a voltage-sensitive dye with good solubility, strong membrane binding and high sensitivity. *European Biophysics Journal*, 37(4):509–514, 2008.

[35] Guixue Bu, Heather Adams, Edward J. Berbari, and Michael Rubart. Uniform action potential repolarization within the sarcolemma of in situ ventricular cardiomyocytes. *Biophysical Journal*, 96(6):2532–2546.

[36] Jesse D. Marshall and Mark J. Schnitzer. Optical strategies for sensing neuronal voltage using quantum dots and other semiconductor nanocrystals. *ACS Nano*, 7(5):4601–4609, 2013.

[37] Evan W. Miller, John Y. Lin, E. Paxon Frady, Paul A. Steinbach, William B. Kristan, and Roger Y. Tsien. Optically monitoring voltage in neurons by photo-induced electron transfer through molecular wires. *Proceedings of the National Academy of Sciences*, 109(6):2114–2119, 2012.

[38] Clifford R. Woodford, E. Paxon Frady, Richard S. Smith, Benjamin Morey, Gabriele Canzi, Sakina F. Palida, Ricardo C. Araneda, William B. Kristan, Clifford P. Kubiak, Evan W. Miller, and Roger Y. Tsien. Improved pet molecules for optically sensing voltage in neurons. *Journal of the American Chemical Society*, 137(5):1817–1824, 2015.

[39] Guan Cao, Jelena Platisa, Vincent A Pieribone, Davide Raccuglia, Michael Kunst, and Michael N Nitabach. Genetically targeted optical electrophysiology in intact neural circuits. *Cell*, 154(4):904–913, 2013.

[40] Francois St-Pierre, Jesse D. Marshall, Ying Yang, Yiyang Gong, Mark J. Schnitzer, and Michael Z. Lin. High-fidelity optical reporting of neuronal electrical activity with an ultrafast fluorescent voltage sensor. *Nat Neurosci*, 17(6):884–889, 2014.

[41] Joel M. Kralj, Adam D. Douglass, Daniel R. Hochbaum, Dougal Maclaurin, and Adam E. Cohen. Optical recording of action potentials in mammalian neurons using a microbial rhodopsin. *Nat Meth*, 9(1):90–95, 2012.

[42] Daniel R. Hochbaum, Yongxin Zhao, Samouil L. Farhi, Nathan Klapoetke, Christopher A. Werley, Vikrant Kapoor, Peng Zou, Joel M. Kralj, Dougal Maclaurin, Niklas Smedemark-Margulies, Jessica L. Saulnier, Gabriella L. Boulting, Christoph Straub, Yong Ku Cho, Michael Melkonian, Gane Ka-Shu Wong, D. Jed Harrison, Venkatesh N. Murthy, Bernardo L. Sabatini, Edward S. Boyden,

Robert E. Campbell, and Adam E. Cohen. All-optical electrophysiology in mammalian neurons using engineered microbial rhodopsins. *Nat Meth*, 11(8):825–833, 2014.

[43] Walther Akemann, Chenchen Song, Hiroki Mutoh, and Thomas KnÃűpfel. Route to genetically targeted optical electrophysiology: development and applications of voltage-sensitive fluorescent proteins. *Neurophotonics*, 2(2):021008–021008, 2015.

[44] Tsai-Wen Chen, Trevor J. Wardill, Yi Sun, Stefan R. Pulver, Sabine L. Renninger, Amy Baohan, Eric R. Schreiter, Rex A. Kerr, Michael B. Orger, Vivek Jayaraman, Loren L. Looger, Karel Svoboda, and Douglas S. Kim. Ultrasensitive fluorescent proteins for imaging neuronal activity. *Nature*, 499(7458):295–300, 2013.

[45] Masatoshi Inoue, Atsuya Takeuchi, Shin-ichiro Horigane, Masamichi Ohkura, Keiko Gengyo-Ando, Hajime Fujii, Satoshi Kamijo, Sayaka Takemoto-Kimura, Masanobu Kano, Junichi Nakai, Kazuo Kitamura, and Haruhiko Bito. Rational design of a high-affinity, fast, red calcium indicator r-camp2. *Nat Meth*, 12(1):64–70, 2015.

[46] Karl Deisseroth. Optogenetics: 10 years of microbial opsins in neuroscience. *Nat Neurosci*, 18(9):1213–1225, 2015.

[47] Adam M. Packer, Botond Roska, and Michael Hausser. Targeting neurons and photons for optogenetics. *Nat Neurosci*, 16(7):805–815, 2013.

[48] Mikhail G. Shapiro, Kazuaki Homma, Sebastian Villarreal, Claus-Peter Richter, and Francisco Bezanilla. Infrared light excites cells by changing their electrical capacitance. *Nat Commun*, 3:736, 2012.

[49] Heng Huang, Savas Delikanli, Hao Zeng, Denise M. Ferkey, and Arnd Pralle. Remote control of ion channels and neurons through magnetic-field heating of nanoparticles. *Nat Nano*, 5(8):602–606, 2010.

[50] Michael J. Caterina, Mark A. Schumacher, Makoto Tominaga, Tobias A. Rosen, Jon D. Levine, and David Julius. The capsaicin receptor: a heat-activated ion channel in the pain pathway. *Nature*, 389(6653):816–824, 1997.

[51] Yung-An Huang, Chun-Wei Kao, Kuang-Kai Liu, Hou-Syun Huang, Ming-Han Chiang, Ching-Ren Soo, Huan-Cheng Chang, Tzai-Wen Chiu, Jui-I. Chao, and Eric Hwang. The effect of fluorescent nanodiamonds on neuronal survival and morphogenesis. *Scientific Reports*, 4:6919, 2014.

[52] Marcus W. Doherty, Neil B. Manson, Paul Delaney, Fedor Jelezko, Jörg Wrachtrup, and Lloyd C. L. Hollenberg. The nitrogen-vacancy colour centre in diamond. *Physics Reports*, 528(1):1–45, 2013.

[53] M. W. Doherty, N. B. Manson, P. Delaney, and L. C. L. Hollenberg. The negatively charged nitrogen-vacancy centre in diamond: the electronic solution. *New Journal of Physics*, 13(2):025019, 2011.

[54] T. Gaebel, M. Domhan, C. Wittmann, I. Popa, F. Jelezko, J. Rabeau, A. Greentree, S. Prawer, E. Trajkov, P. R. Hemmer, and J. Wrachtrup. Photochromism in single nitrogen-vacancy defect in diamond. *Applied Physics B*, 82(2):243–246, 2006.

[55] N. Aslam, G. Waldherr, P. Neumann, F. Jelezko, and J. Wrachtrup. Photo-induced ionization dynamics of the nitrogen vacancy defect in diamond investigated by single-shot charge state detection. *New Journal of Physics*, 15(1):013064, 2013.

[56] Bernhard Grotz, Moritz V. Hauf, Markus Dankerl, Boris Naydenov, Sebastien Pezzagna, Jan Meijer, Fedor Jelezko, Jörg Wrachtrup, Martin Stutzmann, Friedemann Reinhard, and Jose A. Garrido. Charge state manipulation of qubits in diamond. *Nat Commun*, 3:729, 2012.

[57] S. Felton, A. M. Edmonds, M. E. Newton, P. M. Martineau, D. Fisher, and D. J. Twitchen. Electron paramagnetic resonance studies of the neutral nitrogen vacancy in diamond. *Physical Review B*, 77(8):081201, 2008.

[58] Martin Berthel, Oriane Mollet, Gèraldine Dantelle, Thierry Gacoin, Serge Huant, and Aurèlien Drezet. Photophysics of single nitrogen-vacancy centers in diamond nanocrystals. *Physical Review B*, 91(3):035308, 2015.

[59] C. Schreyvogel, V. Polyakov, R. Wunderlich, J. Meijer, and C. E. Nebel. Active charge state control of single nv centres in diamond by in-plane al-schottky junctions. *Scientific Reports*, 5:12160, 2015.

[60] Moritz V. Hauf, Patrick Simon, Nabeel Aslam, Matthias Pfender, Philipp Neumann, Sèbastien Pezzagna, Jan Meijer, Jörg Wrachtrup, Martin Stutzmann, Friedemann Reinhard, and Josè A. Garrido. Addressing single nitrogen-vacancy centers in diamond with transparent in-plane gate structures. *Nano Letters*, 14(5):2359–2364, 2014.

[61] M. V. Hauf, B. Grotz, B. Naydenov, M. Dankerl, S. Pezzagna, J. Meijer, F. Jelezko, J. Wrachtrup, M. Stutzmann, F. Reinhard, and J. A. Garrido. Chemical control of the charge state of nitrogen-vacancy centers in diamond. *Physical Review B*, 83(8):081304, 2011.

[62] M. S. Grinolds, S. Hong, P. Maletinsky, L. Luan, M. D. Lukin, R. L. Walsworth, and A. Yacoby. Nanoscale magnetic imaging of a single electron spin under ambient conditions. *Nat Phys*, 9(4):215–219, 2013.

[63] Fazhan Shi, Qi Zhang, Pengfei Wang, Hongbin Sun, Jiarong Wang, Xing Rong, Ming Chen, Chenyong Ju, Friedemann Reinhard, Hongwei Chen, JÃűrg

Wrachtrup, Junfeng Wang, and Jiangfeng Du. Single-protein spin resonance spectroscopy under ambient conditions. *Science*, 347(6226):1135–1138, 2015.

[64] Stephen J. DeVience, Linh M. Pham, Igor Lovchinsky, Alexander O. Sushkov, Nir Bar-Gill, Chinmay Belthangady, Francesco Casola, Madeleine Corbett, Huiliang Zhang, Mikhail Lukin, Hongkun Park, Amir Yacoby, and Ronald L. Walsworth. Nanoscale nmr spectroscopy and imaging of multiple nuclear species. *Nat Nano*, 10(2):129–134, 2015.

[65] H. J. Mamin, M. Kim, M. H. Sherwood, C. T. Rettner, K. Ohno, D. D. Awschalom, and D. Rugar. Nanoscale nuclear magnetic resonance with a nitrogen-vacancy spin sensor. *Science*, 339(6119):557–560, 2013.

[66] Rugar D., H. J. Mamin, M. H. Sherwood, Kim M., C. T. Rettner, Ohno K.1, and D. D. Awschalom. Proton magnetic resonance imaging using a nitrogenâĂŞvacancy spin sensor. *Nat Nano*, 10(2):120–124, 2015.

[67] V. M. Acosta, E. Bauch, M. P. Ledbetter, A. Waxman, L. S. Bouchard, and D. Budker. Temperature dependence of the nitrogen-vacancy magnetic resonance in diamond. *Physical Review Letters*, 104(7):070801, 2010.

[68] Florian Dolde, Marcus W. Doherty, Julia Michl, Ingmar Jakobi, Boris Naydenov, Sebastien Pezzagna, Jan Meijer, Philipp Neumann, Fedor Jelezko, Neil B. Manson, and Jörg Wrachtrup. Nanoscale detection of a single fundamental charge in ambient conditions using the NV^- center in diamond. *Physical Review Letters*, 112(9):097603, 2014.

[69] B. J. Shields, Q. P. Unterreithmeier, N. P. de Leon, Park H., and M. D Lukin. Efficient readout of a single spin state in diamond via spin-to-charge conversion. *Physical Review Letters*, 114(13):136402, 2015.

[70] Paul A. Nistor, Paul W. May, Francesco Tamagnini, Andrew D. Randall, and Maeve A. Caldwell. Long-term culture of pluripotent stem-cell-derived human neurons on diamond âĂŞ a substrate for neurodegeneration research and therapy. *Biomaterials*, 61:139–149, 2015.

[71] Tzu-Chia Hsu, Kuang-Kai Liu, Huan-Cheng Chang, Eric Hwang, and Jui-I. Chao. Labeling of neuronal differentiation and neuron cells with biocompatible fluorescent nanodiamonds. *Scientific Reports*, 4:5004, 2014.

[72] Ying Zhu, Jing Li, Wenxin Li, Yu Zhang, Xiafeng Yang, Nan Chen, Yanhong Sun, Yun Zhao, Chunhai Fan, and Qing Huang. The biocompatibility of nanodiamonds and their application in drug delivery systems. *Theranostics*, 2(3):302–312, 2012.

[73] Vadym N. Mochalin, Olga Shenderova, Dean Ho, and Yury Gogotsi. The properties and applications of nanodiamonds. *Nat Nano*, 7(1):11–23, 2012.

[74] Eva Rittweger, Kyu Young Han, Scott E. Irvine, Christian Eggeling, and Stefan W. Hell. Sted microscopy reveals crystal colour centres with nanometric resolution. *Nat Photon*, 3(3):144–147, 2009.

[75] Edward H. Chen, Ophir Gaathon, Matthew E. Trusheim, and Dirk Englund. Wide-field multispectral super-resolution imaging using spin-dependent fluorescence in nanodiamonds. *Nano Letters*, 13(5):2073–2077, 2013.

[76] L. P. McGuinness, Yan Y., Stacey A., D. A. Simpson, L. T. Hall, Maclaurin D., Prawer S., Mulvaney P., Wrachtrup J., Caruso F., R. E. Scholten, and L. C. L. Hollenberg. Quantum measurement and orientation tracking of fluorescent nanodiamonds inside living cells. *Nat Nano*, 6(6):358–363, 2011.

[77] Hsin-Hung Lin, Hsiao-Wen Lee, Ruey-Jen Lin, Chih-Wei Huang, Yi-Chun Liao, Yit-Tsong Chen, Jim-Min Fang, Te-Chang Lee, Alice L. Yu, and Huan-Cheng Chang. Tracking and finding slow-proliferating/quiescent cancer stem cells with fluorescent nanodiamonds. *Small*, pages n/a–n/a, 2015.

[78] David A. Simpson, Amelia J. Thompson, Mark Kowarsky, Nida F. Zeeshan, Michael S. J. Barson, Liam T. Hall, Yan Yan, Stefan Kaufmann, Brett C. Johnson, Takeshi Ohshima, Frank Caruso, Robert E. Scholten, Robert B. Saint, Michael J. Murray, and Lloyd C. L. Hollenberg. In vivo imaging and tracking of individual nanodiamonds in drosophila melanogaster embryos. *Biomedical Optics Express*, 5(4):1250–1261, 2014.

[79] D. Le Sage, K. Arai, D. R. Glenn, S. J. DeVience, L. M. Pham, L. Rahn-Lee, M. D. Lukin, A. Yacoby, A. Komeili, and R. L. Walsworth. Optical magnetic imaging of living cells. *Nature*, 496(7446):486–489, 2013.

[80] David R. Glenn, Kyungheon Lee, Hongkun Park, Ralph Weissleder, Amir Yacoby, Mikhail D. Lukin, Hakho Lee, Ronald L. Walsworth, and Colin B. Connolly. Single-cell magnetic imaging using a quantum diamond microscope. *Nat Meth*, 12(8):736–738, 2015.

[81] G. Kucsko, P. C. Maurer, N. Y. Yao, M. Kubo, H. J. Noh, P. K. Lo, H. Park, and M. D. Lukin. Nanometre-scale thermometry in a living cell. *Nature*, 500(7460):54–58, 2013.

[82] Liam T. Hall, Charles D. Hill, Jared H. Cole, Brigitte StÃd'dler, Frank Caruso, Paul Mulvaney, Jörg Wrachtrup, and Lloyd C. L. Hollenberg. Monitoring ion-channel function in real time through quantum decoherence. *Proceedings of the National Academy of Sciences*, 107(44):18777–18782, 2010.

[83] Stefan Kaufmann, David A. Simpson, Liam T. Hall, Viktor Perunicic, Philipp Senn, Steffen Steinert, Liam P. McGuinness, Brett C. Johnson, Takeshi Ohshima, Frank Caruso, Jörg Wrachtrup, Robert E. Scholten, Paul Mulvaney, and Lloyd

Hollenberg. Detection of atomic spin labels in a lipid bilayer using a single-spin nanodiamond probe. *Proceedings of the National Academy of Sciences*, 110(27):10894–10898, 2013.

[84] Zhiqin Chu, Silu Zhang, Bokai Zhang, Chunyuan Zhang, Chia-Yi Fang, Ivan Rehor, Petr Cigler, Huan-Cheng Chang, Ge Lin, Renbao Liu, and Quan Li. Unambiguous observation of shape effects on cellular fate of nanoparticles. *Scientific Reports*, 4:4495, 2014.

[85] Brian Y. Chow, Xue Han, Allison S. Dobry, Xiaofeng Qian, Amy S. Chuong, Mingjie Li, Michael A. Henninger, Gabriel M. Belfort, Yingxi Lin, Patrick E. Monahan, and Edward S. Boyden. High-performance genetically targetable optical neural silencing by light-driven proton pumps. *Nature*, 463(7277):98–102, 2010.